LUND UNIVERSITY

Thermally and Optically Excited Electron Transport in Semiconductor Nanowires

Chen, I-Ju

2018

Document Version:
Publisher's PDF, also known as Version of record

Link to publication

Citation for published version (APA):
Chen, I.-J. (2018). *Thermally and Optically Excited Electron Transport in Semiconductor Nanowires*. [Doctoral Thesis (compilation), Faculty of Engineering, LTH]. Division of Solid State Physics, Lund University, Box 118, SE-221 00 Lund, Sweden,.

Total number of authors:
1

General rights
Unless other specific re-use rights are stated the following general rights apply:
Copyright and moral rights for the publications made accessible in the public portal are retained by the authors and/or other copyright owners and it is a condition of accessing publications that users recognise and abide by the legal requirements associated with these rights.
• Users may download and print one copy of any publication from the public portal for the purpose of private study or research.
• You may not further distribute the material or use it for any profit-making activity or commercial gain
• You may freely distribute the URL identifying the publication in the public portal

Read more about Creative commons licenses: https://creativecommons.org/licenses/

Take down policy
If you believe that this document breaches copyright please contact us providing details, and we will remove access to the work immediately and investigate your claim.

LUND UNIVERSITY

PO Box 117
221 00 Lund
+46 46-222 00 00

Download date: 18. May. 2025

Thermally and Optically Excited Electron Transport in Semiconductor Nanowires

I-JU CHEN
FACULTY OF ENGINEERING | LUND UNIVERSITY

Thermally and Optically Excited Electron Transport in Semiconductor Nanowires

Thermally and Optically Excited Electron Transport in Semiconductor Nanowires

I-Ju Chen

LUND UNIVERSITY

DOCTORAL DISSERTATION
by due permission of the Faculty of Engineering, Lund University, Sweden.
To be defended on Wednesday, the 12th of Septermber, at 13:15 in the Rydberg Lecture Hall at the Department of Physics, Sölvegatan 14, Lund

Faculty opponent
Assoc. Prof. Ilaria Zardo

University of Basel, Switzerland

Organization LUND UNIVERSITY Division of Solid State Physics Department of Physics P.O. Box 118, SE-221 00 Lund, Sweden	Document name DOCTORAL DISSERTATION
	Date of issue
Author: I-Ju Chen	Sponsoring organization

Title: Thermally and Optically Excited Electron Transport in Semiconductor Nanowires

Abstract:

This thesis explores the transport of thermally and optically excited electrons in various nanowire structures. On one hand, electrons are thermally excited when the temperature is nonzero, and the thermal energy help them surmount energy barriers that are present in the material. On the other hand, when the electron distributions at different part of the material are out-of-equilibrium due to thermal or optical excitations, an electrical current is created, converting the thermal and optical energy into electricity. Thus, in this thesis, the transport of thermally and optically excited electrons is studied to extract the electronic properties of nanowire heterostructures and to investigate the limit of energy conversion in thermoelectric and photovoltaic devices.

First, the measurement of thermionic emission current, which is the thermally induced electron flow over energy barriers, is used to study the electronic properties of InAs crystal phase heterostructures. The band offset, polarization charges, and carrier density differences between the zinc blende and wurtzite crystal phases are investigated. In addition, quantum dot states can be formed within a wurtzite segment or between two closely spaced wurtzite segments in an otherwise zinc blende nanowire. The quantum dot formed between two wurtzite segments can be further split into two parallel coupled quantum dots. Numerical simulations are used to understand the formation and the interaction between the two quantum dots.

Secondly, the thermoelectric response of pure zinc blende InAs nanowires is studied. At low temperatures, the quantum confinement effect can be observed, and the electrons exhibit quasi-1D transport. Conductance quantization and Seebeck coefficient oscillation as a function of gate voltages, characteristic of quasi-1D system, are observed. More importantly, a theoretical limit for the power factor of non-ballistic 1D channels is found and tested experimentally.

Finally, the transport of optically excited electrons in InAs-InP-InAs heterostructure nanowires is studied. Electron distributions that are out-of- thermal equilibrium with, more specifically hotter than, the lattice and the environment are created through optical excitation with photon energies significantly larger than the band gap. An energy barrier formed by the InP segment is used to selectively extract high energy electrons and convert their kinetic energy into electrical potential. Nanophotonic effects including optical resonances in nanowires and localized surface plasmon resonances in metal nanostructures are used to create a nonuniform hot-electron distribution around the InP barrier. In particular, the hot-electrons can be generated locally near the controlled position of the plasmonic metal nanostructures, which facilitates an in-depth study of their transport.

Key words: InAs, InP, nanowire, thermoelectric, hot-carrier solar cell		
Classification system and/or index terms (if any)		
Supplementary bibliographical information		Language: English
ISSN and key title		ISBN: 978-91-7753-794-6
Recipient's notes	Number of pages 154	Price
	Security classification	

I, the undersigned, being the copyright owner of the abstract of the above-mentioned dissertation, hereby grant to all reference sources permission to publish and disseminate the abstract of the above-mentioned dissertation.

Signature I-Ju Chen Date 2018-08-15

Thermally and Optically Excited Electron Transport in Semiconductor Nanowires

I-Ju Chen

Front Cover: Offset electrical conductance quantization curves measured in a InAs single nanowire device decorated with blocks of colors.

Back Cover: Thermoelectric power generation from the same device as a function of the back-gate voltages. The data points are composed of two states of cat.

Copyright pp 1-64 © 2018 I-Ju Chen

Paper I, II, IV © 2017 American Chemical Society

Paper III © 2018 American Physical Society

Paper V © 2018 the authors

Division of Solid State Physics
Department of Physics
Lund University
P.O. Box 118
SE-221 00 Lund
Sweden

ISBN 978-91-7753-794-6 (print)
ISBN 978-91-7753-795-3 (pdf)

Printed in Sweden by Media-Tryck, Lund University
Lund 2018

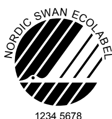

Media-Tryck is an environmentally certified and ISO 14001 certified provider of printed material. Read more about our environmental work at www.mediatryck.lu.se

To Pierre-Adrien

Table of Contents

Acknowledgement iii
Abstract v
Popular Science Summary vii
List of publications ix
Abbreviations xi
Symbols xiii
Chapter 1 Introduction 1
1.1 Electron flow in crystals 1
1.2 III-V semiconductor nanowires 3
Chapter 2 Nanowire device fabrication and measurement 7
2.1 The nanowire material 7
2.2 Metal-oxide-semiconductor nanowire field-effect transistor 9
2.3 Thermoelectric measurement 11
2.4 Scanning probe thermometry 13
2.5 Photocurrent-voltage measurement 15
Chapter 3 Electron transport in nanowire polytypic heterostructures 17
3.1 Polytypism in semiconductor nanowires 17
3.2 Band diagram of InAs ZB/WZ heterostructures 18
3.3 Semiclassical transport in InAs ZB/WZ heterostructures 21
3.4 Quantum transport in InAs ZB/WZ heterostructures 26
Chapter 4 Thermoelectric effect in 1D nanowires 31
4.1 Thermoelectric effect 31
4.2 Size effects in nanowires 33
4.3 Thermoelectric coefficient of quasi-1D systems 37

Chapter 5 Photo-excited hot-carrier effect in nanowire heterostructures 41
5.1 Hot-carrier based optoelectronic devices 41
5.2 Optical effects in nanowire-based structures...42
5.3 Photo-excited carrier dynamics 48
5.4 Photo-excited carrier transport 49
Chapter 6 Conclusion and outlook 55
Bibliography 57

Acknowledgement

I would like to express my deep appreciation of everyone that has helped me with my PhD education and the research projects in this thesis.

First and foremost I want to thank my supervisor Claes Thelander for being such a great supervisor. You have taught me so much with your physical knowledge, pragmatic approach, and work ethics. You helped me when I didn't even know how to ask for help. To my co-supervisor Heiner Linke, I am grateful for the opportunities you gave me, including collaborations, internship, and conference participation. And I am always very inspired by your broader, more ambitious and strategic perspectives. You really taught me to think outside the box. To my third supervisor, Mats-Erik Pistol, you have shown me by example how to think like there is no box. I really appreciate your ever friendly and empathetic support.

I thank Kimberly Dick for your comments on this thesis, your valuable inputs on various manuscripts and projects, and the nanowires that are provided by your team. I thank Rong Sun, Luna Namazi, and Sebastian Lehmann for providing the nanowires in this thesis. Also to Sebastian Lehmann, I am thankful for all your help with nanowire imaging and expert opinion on nanowire crystal structures.

I am grateful for having Malin Nilsson, Adam Burke, Steven Limpert, and Artis Svilans as my closest collaborators. The exchanges with you have been really helpful and gave me plenty of new ideas.

I would like to thank Pyry Kivisaari and Steven Limpert for answering all my questions about numerical simulations and sharing with me your tips.

I also want to express my gratitude to Federico Capasso for your insightful perspectives about our hot-carrier projects.

Many thanks to my office mates, Vilgaile Dagyte, Xulu Zeng, Marcus Tornberg, Si Hoai Trung Tran, and Artis Svilans for the good office atmosphere and all the timely help with physics, software, and administrative questions.

I would like to thank the NanoLab staff members, Maria Huffman, Ivan Maximov, Mariusz Graczyk, Sara Ataran, George Rydnemalm, Håkan Lapovski, Dmitry Suyatin, Peter Blomqvist and David Fitzgerald, for the great lab condition and support. I am also thankful to the technical and administrative staff of solid state physics, Dan Hessman, Anneli Lövgren, Anders Gustavsson, Line Lundfald, Johanna Mosgeller and many more, for keeping our department running.

I also want to say thank you to senior staff members, Martin Leijnse, Lars Samuelsson, Peter Samuelsson, Anders Mikkelsen, Adam Burke, and Ville Maisi, who have helped me in various ways. Moreover, I am grateful for being able to work alongside my great colleagues in FTF, Laura Abariute, Jonatan Fast, David Göransson, Martin Josefsson, Maryam Khalilian, Zhen Li, Frida Lindberg, Sara Thorberg, Neimantas Vainorius, Damiano Verardo, Florinda Viñas Boström, Chunlin Yu, Heidi Potts, Marcelo Alcocer, Felix Vennberg, Markus Snellman and many more.

I also want to express my appreciation of people in the Materials Integration and Nanoscale Devices group at IBM, Zurich for kindly welcoming and helping me during my internship. I want to thank the group manager Kirsten Moselund for welcoming me to your group and all the support during the internship. To Bernd Gotsmann, I thank you for being a great project supervisor. I am really inspired by your broad interest in research. I also want to thank Fabian Könemann for teaching me about the scanning probe thermometry techniques, and always having a good energy.

I am deeply thankful for my family. Knowing that you care about me and that I can always rely on you is the best feeling. I also want to thank the Mante family, which has become my second family during my PhD, for all the good times we share.

Finally, to my husband Pierre-Adrien Mante, I am so grateful for having you to explore physics, life and the world with me.

Abstract

This thesis explores the transport of thermally and optically excited electrons in various nanowire structures. On one hand, electrons are thermally excited when the temperature is nonzero, and the thermal energy help them surmount energy barriers that are present in the material. On the other hand, when the electron distributions at different part of the material are out-of-equilibrium due to thermal or optical excitations, an electrical current is created, converting the thermal and optical energy into electricity. Thus, in this thesis, the transport of thermally and optically excited electrons is studied to extract the electronic properties of nanowire heterostructures and to investigate the limit of energy conversion in thermoelectric and photovoltaic devices.

First, the measurement of thermionic emission current, which is the thermally induced electron flow over energy barriers, is used to study the electronic properties of InAs crystal phase heterostructures. The band offset, polarization charges, and carrier density differences between the zinc blende and wurtzite crystal phases are investigated. In addition, quantum dot states can be formed within a wurtzite segment or between two closely spaced wurtzite segments in an otherwise zinc blende nanowire. The quantum dot formed between two wurtzite segments can be further split into two parallel coupled quantum dots. Numerical simulations are used to understand the formation and the interaction between the two quantum dots.

Secondly, the thermoelectric response of pure zinc blende InAs nanowires is studied. At low temperatures, the quantum confinement effect can be observed, and the electrons exhibit quasi-1D transport. Conductance quantization and Seebeck coefficient oscillation as a function of gate voltages, characteristic of quasi-1D system, are observed. More importantly, a theoretical limit for the power factor of non-ballistic 1D channels is found and tested experimentally.

Finally, the transport of optically excited electrons in InAs-InP-InAs heterostructure nanowires is studied. Electron distributions that are out-of- thermal

equilibrium with, more specifically hotter than, the lattice and the environment are created through optical excitation with photon energies significantly larger than the band gap. An energy barrier formed by the InP segment is used to selectively extract high energy electrons and convert their kinetic energy into electrical potential. Nanophotonic effects including optical resonances in nanowires and localized surface plasmon resonances in metal nanostructures are used to create a nonuniform hot-electron distribution around the InP barrier. In particular, the hot-electrons can be generated locally near the controlled position of the plasmonic metal nanostructures, which facilitates an in-depth study of their transport.

Popular Science Summary

Fascinated by mysterious phenomena, such as the forces produced by rubbing a piece of cloth on amber and lodestones that attract iron, early scientists and engineers set out to explore the laws of electrical and magnetic phenomena. In the 16th century, the scientific method had been established and used to study these phenomena, first by Williams Gilbert. Thanks to the discoveries and inventions by many scientist, such as Alessandro Volta's electrical battery and Michael Faraday's electrical motor and generator, a unified theory of electromagnetics was put forward by James Clerk Maxwell in 1873 [1]. The theory not only explains all the electrical and magnetic phenomena observed to that time, but also predicted many more.

With the ever-improving understanding of electricity and magnetism, there is a burgeoning of electromagnetic technologies at the turn of the 19th century, including the telephone, radio communication systems, electrical power generators, electrical motors, and the electric-powered incandescent light. However, the nature of electricity remains a mystery. What is the carrier of the electric current? In the 19th century, many experiments on the electrical discharge in vacuum tubes were carried out to answer this mystery. Finally, negatively charged particles with mass 1/1837 that of an atom, thereafter named *electrons*, were widely accepted as the most basic carrier of electric current after Joseph John Thomson announced the result of his carefully conducted experiment in 1897 [1]. Quickly thereafter, the development of vacuum tube electronic devices enabled many applications, including the radio, television, radar, and computer in the early 20th century.

However, vacuum tube electronic devices were limited by problems such as high cost, breakability, cumulative size and power consumption. Meanwhile, the study of semiconductor physics were just falling into places: electron transport in solid could be understood through the band theory derived from quantum mechanics [2]. Based on the theoretical understanding and the capability to grow purer semiconductors, transistors were created by John Bardeen, Walter Brattain, and William Shockley in Bell lab. During this time, light-induced current was also

observed in semiconductor p-n junctions, which later became the foundation of photovoltaic solar cells.

Semiconductor electronics soon gave birth to many more applications including the laser diode and LED. All these applications rely on the capability to manipulate the composition of semiconductors to control the transport of electrons. Gradually, it became possible to change the composition of semiconductors on the scale of a nanometer (a billionth of a meter). As of today, semiconductors can take many nanoscale 3D shapes: nanowires, quantum dots, nanosails, etc., either through top-down or bottom-up fabrication approaches. Electron transport is drastically modified in these nanostructures, which brings many new possibilities accompanied by as many puzzles.

In this thesis, we investigated electron transport in semiconductor nanowires under the influence of light and heat. When light and heat are used to drive the electrical current, their optical and thermal energy can be converted into electrical energy, which are the physical principles behind sustainable energy technologies such as solar cells and thermoelectric generators. Because nanowires can have different crystal, optical, thermal, and electrical properties compared to bulk semiconductors, they provide new possibilities to make these energy conversion processes more efficient. The results of this thesis are some steps taken to better understand the electronic properties of nanowires and the limit of energy conversion. First, we studied electron transport in nanowires with crystal structures that exclusively form in the nanoscale. Secondly, we tested the fundamental limit of converting thermal energy into electricity. Finally, we build a new type of solar energy conversion device based on nanoscale optical and electron transport effects.

List of publications

I. **Conduction band offset and polarization effects in InAs nanowire polytype junctions**
I-Ju Chen, Sebastian Lehmann, Malin Nilsson, Pyry Kivisaari, Heiner Linke, Kimberly A. Dick, and Claes Thelander
Nano Letters, 17 (2), 902-908, 2017

I fabricated the devices with M. Nilsson. I performed the experiment and data analysis. I performed the numerical simulations with help from P. Kivisaari. I wrote the manuscript with help from the coauthors.

II. **Parallel-coupled quantum dots in InAs nanowires**
Malin Nilsson, I-Ju Chen, Sebastian Lehmann, Vendula Maulerova, Kimberly A. Dick, and Claes Thelander
Nano Letters, 17 (12), 7847-7852, 2017

I performed the numerical simulations, participated in interpreting the underlying physical mechanism, and provided input to the manuscript.

III. **Thermoelectric power factor limit of a 1D nanowire**
I-Ju Chen, Adam Burke, Artis Svilans, Heiner Linke, and Claes Thelander
Physical Review Letter, 120, 177703, 2018

I planned and coordinated the study, fabricated the devices, and performed the experiments. I analyzed the data and wrote the manuscript with help from the coauthors.

IV. **Bipolar photothermoelectric effect across energy filters in single nanowires**

Steven Limpert, Adam Burke, I-Ju Chen, Nicklas Anttu, Sebastian Lehmann, Sofia Fahlvik, Stephen Bremner, Gavin Conibeer, Claes Thelander, Mats-Erik Pistol, and Heiner Linke
Nano letters 17 (7), 4055-4060, 2017

I participated in the device fabrication and building the setup, and provided input to the manuscript.

V. **Extraction of thermal and non-thermal hot-carriers in nanowire-metal nano-antenna devices**
I-Ju Chen, Steven Limpert, Wondwosen Metaferia, Claes Thelander, Lars Samuelson, Federico Capasso, Adam Burke, and Heiner Linke
Manuscript

I fabricated the devices, performed the experiments and data analysis. I performed the numerical simulation with help from S. Limpert. I wrote the manuscript with help from the coauthors.

The following papers are not included in the thesis

VI. **Sn-seeded GaAs nanowires as self-assembled radial p–n junctions**
Rong Sun, Daniel Jacobsson, I-Ju Chen, Malin Nilsson, Claes Thelander, Sebastian Lehmann, and Kimberly A. Dick
Nano Lett., 15, 3757, 2015

VII. **Single-nanowire, low-bandgap hot carrier solar cells with tunable open-circuit voltage**
Steven Limpert, Adam Burke, I-Ju Chen, Nicklas Anttu, Sebastian Lehmann, Sofia Fahlvik, Stephen Bremner, Gavin Conibeer, Claes Thelander, Mats-Erik Pistol, and Heiner Linke
Nanotechnology 28 (43), 434001, 2017

VIII. **Confinement effects on Brillouin scattering in semiconductor nanowire photonic crystal**
Pierre-Adrien Mante, Nicklas Anttu, Wei Zhang, Jesper Wallentin, I-Ju Chen, Sebastian Lehmann, Magnus Heurlin, Magnus T Borgström, Mats-Erik Pistol, Arkady Yartsev
Physical Review B 94 (2), 024115, 2016

Abbreviations

AlAs	Aluminium Arsenide
CBE	Chemical Beam Epitaxy
EBL	Electron Beam Lithography
ECCI	Electron Channelling Contrast Imaging
GaAs	Gallium Arsenide
Ge	Germanium
InAs	Indium arsenide
InP	Indium phosphide
MOSFET	Metal Oxide Semiconductor Field Effect Transistor
MOVPE	Metal Oxide Vapour Phase Epitaxy
QD	Density Functional Theory
SEM	Scanning Electron Microscope
Si	Silicon
SiO_2	Silicon Dioxide
TEM	Transmission Electron Microscope
WZ	Wurtzite
ZB	Zinc blende

Symbols

Fundamental constant

e	Elementary charge	1.602×10^{-19} C
h	Planck constant	6.626×10^{-34} J s
$\hbar$	$h/2\pi$	1.055×10^{-34} J s
k_B	Boltzmann constant	1.381×10^{-23} J/K
m_e	Free electron mass	9.11×10^{-31} kg

Other symbols

ΔT	Temperature difference
E	Energy
$\vec{E}$	Electric field
ε_r	Dielectric function
G	Conductance
I	Electrical current
I_{th}	Thermal current
I_Q	Heat current
J	Electrical current density
L_{WZ}	WZ segment length
m^*	Electron effective mass

μ	Electrochemical potential
S	Seebeck coefficient (thermopower)
S^2G	Power factor
T	Temperature
V_g	Gate voltage
V_{th}	Thermal voltage
ω	Angular frequency

Chapter 1

Introduction

1.1 Electron flow in crystals

In isolated atoms, electrons occupy atomic orbitals around the nucleus. For the electrons to travel across space, an energy larger than the binding energy (or ionization energy) is needed to separate the electrons from the ions. In a crystalline solid, atoms are brought together and arranged in periodic arrays. The atoms are held together by various types of chemical bonds through the interaction of electrons in the outer shells of the atoms, i.e. valence electrons, and the ions [3,4]. Due to these interactions, the discrete atomic levels broaden into bands of electronic levels and the electrons can move inside the crystal. To account for these interactions, electrons in the crystals are often thought of as quasi-particles that have different effective mass than real electrons.

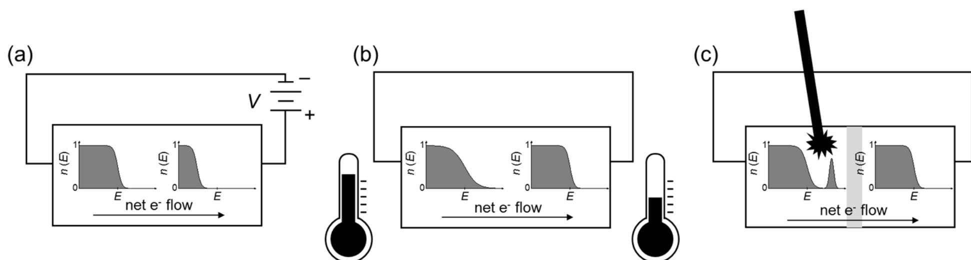

Figure 1.1: Electron energy distribution under nonequilibrium conditions created when (a) the device is connected to a battery, (b) the device is in a temperature gradient, and (c) the device has am asymmetric absorption of light.

In thermodynamic equilibrium, electrons fill these energy levels with an average occupation number given by the Fermi-Dirac distribution

$$f = \frac{1}{e^{\frac{E-\mu}{k_B T}}+1}, \qquad (1.1)$$

with electrochemical potential μ and temperature *T*. When a device is in thermodynamic equilibrium (μ and *T* are constant throughout the whole device), although electrons can move in the crystal, there is no net flow of electrons and energy. Different parts of the device need to be out-of-equilibrium to give rise to electric current. For example, this can be achieved by connecting the device to a battery where the anode has a larger μ than the cathode. Therefore, electrons in the system are no longer in diffusive equilibrium [5] and there will be a net electron flow (Fig. 1.1(a)). Similarly, when there is a temperature gradient in the device, electrons in the system are not in thermal equilibrium. Consequently, there will be a net heat flow, and often also a net electron flow (Fig. 1.1(b)), which leads to the thermoelectric effect. Another situation that can give rise to a net flow is when electrons absorb light and get excited to higher energy levels, where they are out-of-equilibrium with other electrons and the lattice. Additionally if the device has an asymmetric structure or light absorption profile, the optically excited electrons from different parts of the device are out-of-equilibrium and will create a net electron flow (Fig. 1.1(c)), which allows conversion of light into electricity through, for example, photovoltaic and photo-thermoelectric effects.

When an electron travels in a realistic crystal, it can collide with impurities, and excitations such as phonons, photons, or other electrons. Due to these collisions, the initial momentum of the electron is destroyed after some distance, which is called the mean free path [6]. When the device length is comparable to the mean free path, electrons undergo no or few scattering events and the transport is ballistic or quasi-ballistic. In a ballistic conductor, electrons are transmitted with a unitary probability (Fig. 1.2(a)). The scattering events can be separated into inelastic scattering (with phonons, photons, and electrons), which destroys phase coherence, and elastic scattering (with static impurities) that does not. Thus quantum interference effects can occur in devices with length shorter than the phase-relaxation length. In contrast to these mesoscopic transport phenomena, if the device length is much longer than the mean free path and the phase-relaxation length, electrons undergo a series of scattering events as they traverse through the device, which is the regime of diffusive transport. At equilibrium, the trajectory of an electron can be visualized as a random walk. However, in the presence of an electric field $\vec{E}$, the electrons acquire an additional velocity between two scattering events and give rise to a net current density

$$J = \frac{ne^2\tau}{m^*}\vec{E}, \qquad (1.2)$$

with electron density *n*, mass m_e, charge *e*, and scattering time *t* as described by the Drude model (Fig. 1.2(b)).

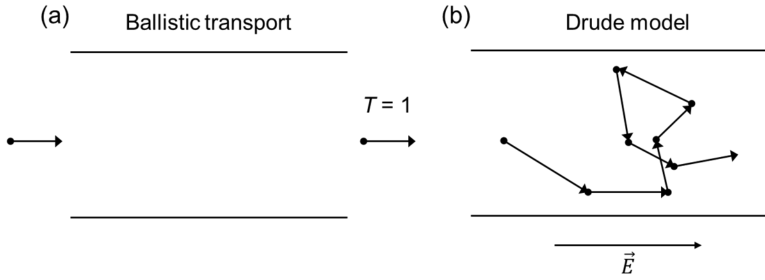

Figure 1.2: Schematic representation of (a) ballistic electron transport viewed as a transmission problem and (b) diffusive electron transport described by the Drude model.

1.2 III-V semiconductor nanowires

Crystals of group IV elements (Si, Ge), III-V and II-V compounds primarily have covalent bonds, where the valence electrons are shared between neighbouring atoms and are not strongly localized near the core ions [4]. These semiconductor materials have electrical conductivity between conductors and insulators, which can be understood from the presence/absence and size of band gap near the Fermi level. In terms of technological applications, Si is the most important semiconductor thanks to it being the 2nd most abundant element in the earth's crust and that the Si-SiO_2 interface can form without a large density of electrically active defects, which are important for the functionality of MOSFETs [7]. III-V compound semiconductors, by offering many complimentary qualities, are probably next in importance to Si. Many of the III-V semiconductors have direct band gaps in the range of the energy of optical and infrared radiation, which are important for optoelectronic applications, and many also have small electron effective mass that leads to high mobility. In addition, several combinations of III-V compounds (GaAs and AlAs) have very close lattice constants. Thus heterostructures of these compounds and their alloys can be used for band engineering.

Since a few decades, III-V semiconductors can be grown in nanowire structures. Nanowires have diameters on the order of a nanometer (10^{-9} meter) and much longer lengths. This slender structure allows some unique material, electronic, thermal, and optical properties, which are central to different studies in this thesis.

First, the nanowire geometry allows for strain relaxation in the lateral directions. Therefore, compared to thin films, nanowires with low defects densities can be grown on different substrates, and heterostructures of lattice-mismatched material combinations can be formed. In addition, in bulk, all III–V compounds except III-N exhibit a cubic zinc blende (ZB) structure, whereas nanowires can contain both

zinc blende and wurtzite (WZ) structures, which are crystal polytypes that have the same in-plane atomic structure but different stacking sequences along the growth direction [8,9]. These small structural differences lead to different electronic band structures for ZB and WZ. The electronic properties of InAs nanowires with ZB/WZ heterostructures are studied in papers I and II.

Second, when the diameters of semiconductor nanowires are comparable to the Fermi wavelength, which is the de Broglie wavelength of electrons at the Fermi energy, the motion of electrons is restricted in the lateral direction, resulting in discrete energy levels. The electrons are only free to move along the nanowire axis. Thus, even though nanowires are 3D objects, the electrons can show quasi-1D transport characteristics. The thermoelectric transport of quasi-1D nanowires is studied in paper III. Furthermore, pairs of tunnel barriers can be introduced in a nanowire, from heterostructures or electrostatic gating, which confine the electrons in all three dimensions to form quantum dots. Quantum dots formed in InAs ZB/WZ nanowire heterostructures are studied in Paper I and II.

Third, the dimensions of nanowires are close to the wavelength of optical and near infrared electromagnetic waves, which result in optical resonance effects [10,11]. The resonance modes can be controlled by tuning the size, geometry, and orientation of the nanowires. They lead to enhanced light absorption in subwavelength structures, which opens up opportunities to realize high-performance nanowire optoelectronic devices. In addition, metallic plasmonic elements can also be integrated to further concentrate the electromagnetic wave in the near field. Optical hot-carrier devices based on nanowires and hybridized nanowire-metal plasmonic antenna structures are studied in Paper IV and Paper V, respectively.

The rest of the thesis is organized as follows:

Chapter 2 introduces the different nanowire materials, nanowire device structures, and measurement techniques that are used in the papers included in this thesis.

Chapter 3 discusses the electronic properties of InAs ZB/WZ nanowire heterostructures. Overall, we find that the ZB/WZ heterojunction has a type-II band alignment. In addition, carrier concentration differences and polarization effects also contribute to the formation of an energy barrier when a WZ segment is present in a ZB InAs nanowire. From temperature-dependent electrical measurements, these effects are assessed quantitatively in paper I. At low temperatures, electron transport through the WZ barrier is dominated by quantum tunnelling; thus quantum dots can be formed in WZ/ZB/WZ heterostructures and probed by transport measurements. The formation of parallel-coupled double quantum dots through electrostatic gating

is studied in paper II. This chapter serves as an introduction to the physical picture behind Paper I and II.

Chapter 4 introduces the thermoelectric effect, focused on the thermoelectric transport properties of quasi-1D electron systems. Observation of quasi-1D electron transport in nanowires requires that the quantum confinement energy is comparable to the Fermi energy and larger than the thermal energy ($k_B T$), and that the nanowire is homogeneous without unintentional formation of bound states. The thermoelectric properties of nanowires that show quasi-1D electron transport are studied in Paper III and an introduction of the theoretical background is given in that chapter.

Chapter 5 gives an introduction to the physical phenomena relevant for the realization of an optical hot-carrier device based on single-nanowire and single-nanowire-metal plasmonic antenna structures studied in Paper IV and V. It includes a description of nanophotonic effects, as well as the generation, relaxation, and transport of the hot-carriers.

Chapter 2

Nanowire device fabrication and measurement

This chapter introduces the nanowire materials covered in the thesis, and also the principle, design, fabrication, and measurement of single-nanowire field-effect transistor devices.

2.1 The nanowire material

The nanowires used in this thesis are grown through epitaxy. Epitaxy is the growth of crystalline materials on crystalline substrates, which determine the crystal structures of the grown materials. The pure and crystal-phase heterostructure InAs nanowires are grown by metal organic vapor phase epitaxy (MOVPE), which is versatile and the most common nanowire growth technique [12]. The InAs/InP heterostructure nanowires are grown by chemical beam epitaxy (CBE), which is suitable for growing heterostructures with sharp interfaces thanks to its lower growth rate and ability to abruptly switch precursors during growth [13].

2.1.1 MOVPE growth of InAs nanowire and InAs crystal-phase heterostructure nanowire

The InAs nanowires in Papers I-III were grown by low pressure MOVPE on (111)B InAs substrates catalyzed by Au aerosols seed particles (40-60 nm) which determine the nanowire diameters. Trimethylindium (TMIn) and arsine (AsH_3) were used as

group-III and group-V precursors. The growth of ZB crystal phase along $[\bar{1}\bar{1}\bar{1}]$ direction and WZ along $[000\bar{1}]$ direction can be precisely controlled by tuning the ratio of III-V precursor flow, the total precursor flow, and the growth temperature [8,14].

In Papers I and II, InAs nanowires with controlled ZB/WZ heterostructures were grown for the study of their electronic properties. The growth temperature (= 470°) and TMIn flow were held constant whilst a higher AsH_3 flow was used to switch the crystal phase from WZ to ZB. In Paper III, nanowires with homogeneous ZB crystal structure are used for the study of one-dimensional electron transport.

The ZB/ WZ heterostructure can be observed by resolving the atomic structure in transmission electron microscopy (TEM) as shown in Fig. 2.1(a). Moreover, electron channelling contrast imaging (ECCI) using scanning electron microscopy (SEM) can also be applied to image the ZB/ WZ heterostructure (Fig. 2.1(b)). In ECCI, electron channelling, which refers to electron propagation deeper into the crystal at specific incident directions [15], allows imaging of the crystallinity through a diffraction contrast. This technique is suited for imaging nanowire devices as it does not require further sample preparation.

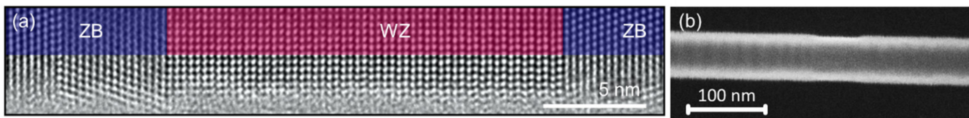

Figure 2.1: (a) High resolution TEM image of the position in the InAs nanowire with the ZB/WZ/ZB crystal structure sequence. (b) Crystal phase resolved by ECCI in the SEM.

2.1.2 CBE growth of InAs/InP heterostructure nanowire

The InAs/InP heterostructure nanowires in Papers IV and V were grown by CBE on InAs (111)B substrates also catalyzed by Au aerosols seed particles (40-60 nm). TMIn, tertiarybutylarsine (TBAs) and tertiarybutylphosphine (TBP) were used as precursors. To switch between InAs and InP, first the TMIn source was switched off, then after 5 s the group-V sources were switched on/off simultaneously, and the TMIn source was switched on again after another 5 s [16]. TEM analysis (Fig. 2.2(a)) shows that the nanowires have WZ crystal structure. The InAs/InP heterostructure can also be resolved with SEM as shown in Fig. 2.2 (b).

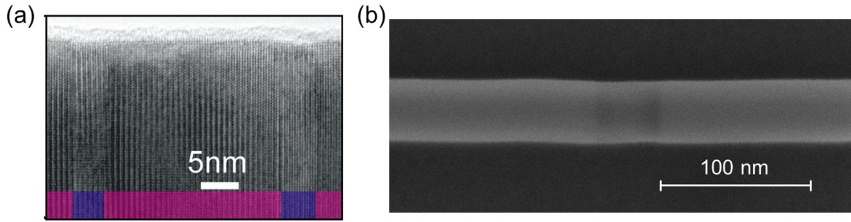

Figure 2.2: (a) InAs nanowire with two thin InP barriers resolved in TEM and (b) InAs nanowire with one InP barrier resolved in SEM.

2.2 Metal-oxide-semiconductor nanowire field-effect transistor

The single-nanowire back-gate metal-oxide-semiconductor field-effect transistor (MOSFET) is a basis for the different devices studied in this thesis. In such devices, the nanowires have Ohmic contacts to the source and drain terminals (Fig. 2.3 (a)), and are capacitively coupled to a back-gate (Fig. 2.3 (b)), which is separated from the nanowires by the Si/SiO_2 substrate. In MOSFETs, when an electrical potential is applied across the gate and source terminal, the induced electric field modifies the electrical conductivity of the conducting channel between the source and drain.

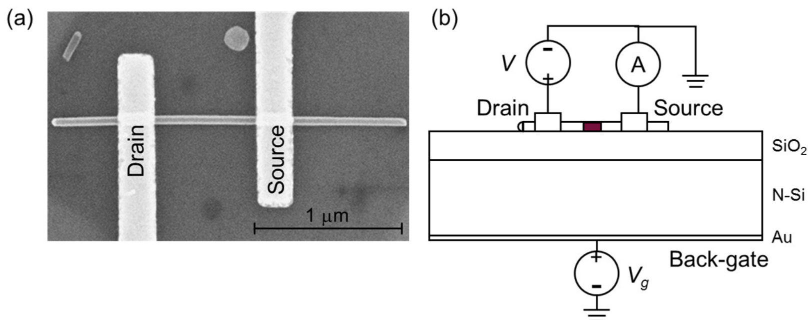

Figure 2.3: (a) SEM of a single-nanowire back-gate MOSFET. (b) Schematics of the side view of the device structure and the electrical measurement circuitry.

2.2.1 Field effect

The nanowire MOSFET structure forms a capacitor, where the gate voltage V_g (Fig. 2.3 (b)) can be used to modify the electrostatic potential and thus the carrier concentration in the semiconductor. Following Gauss's law, the electrostatic potential V is described by Poisson's equation

$$\nabla \cdot (\varepsilon_r \varepsilon_0 \nabla V) = \rho_{tot}, \quad (2.1)$$

with, vacuum permittivity ε_0, dielectric function ε_r, and the total volume charge density

$$\rho_{tot} = e(p - n + N_d^+ - N_a^-), \quad (2.2)$$

where p, n, N_d^+, N_a^- are the hole, electron, ionized acceptor and donor density respectively.

The electron and hole concentrations can be calculated from the density of states ($D(E)$) and the Fermi-Dirac distribution

$$n = \int_0^\infty \frac{1}{e^{\frac{E-\mu}{k_B T}}+1} D(E)\, dE, \quad (2.3)$$

with chemical potential μ. The spatial distribution of the electrostatic potential and carrier concentration as functions of V_g can be obtained from a self-consistent numerical solution of Eq. 2.1-3.

2.2.2 Single-nanowire MOSFET fabrication

The first step to fabricate the devices is to mechanically transfer the nanowires from the growth substrate to a measurement substrate, which is degenerately n-doped Si covered by 100 – 200 nm thick layer of thermally grown SiO_2. The back of the measurement substrate is covered by a Au film, which acts as a back-gate, whereas the front is covered by Au structures that will be used as EBL markers and coordinate references as shown in Fig. 2.4(a,b). These Au structures are fabricated in advance using EBL, UV lithography, and evaporation.

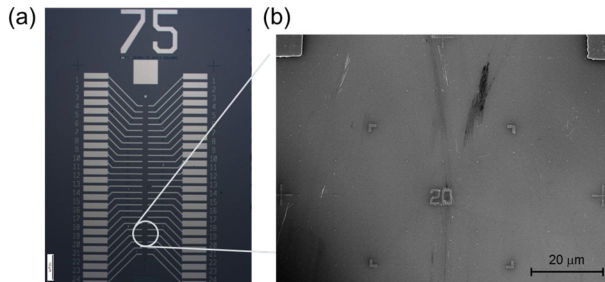

Figure 2.4: A measurement substrate under (a) an optical microscope and (b) an SEM.

Suitable nanowires are identified by low-resolution SEM and selected for device fabrication. Afterwards, the samples are spin-coated with a positive resist, polymethyl methacrylate (PMMA 950 A5), and baked for 10 minutes. Electron beam lithography is used to create openings for the desired metal structures. The

exposed resist is dissolved after immersion in the developer for 45 s. The contact area is first treated with O_2-plasma ashing to remove resist residue. Then the native oxides on the exposed InAs surface is removed by wet etching in either $(NH_4)_2S_x$:H_2O (1:20) for 1 min (Paper I, II, IV, V) or HCl:H_2O (1:10) for 10 s (Paper III). Finally, a film of 25 nm Ni and 75 nm Au is evaporated onto the sample and then lifted off in acetone at up to 55 °C.

2.3 Thermoelectric measurement

For the thermoelectric measurements in Paper III, a Joule heater is added adjacent to one end of the nanowire to create a temperature gradient, and a set of four-probe metal lines is added to both the source and drain contacts for temperature characterization using resistance thermometry (Fig. 2.5 (a,b)).

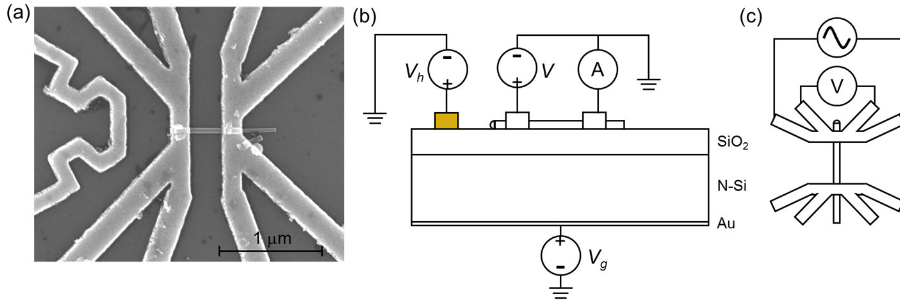

Figure 2.5: (a) SEM of a single-nanowire back-gate MOSFET with a side Joule heater. The source and drain are also four-probe contacts used for resistance thermometry. (b) Side-view schematics of the device structure and the thermoelectric measurement circuitry. (c) Top-view schematics of the resistance thermometry circuit.

2.3.1 Conductance, Seebeck coefficient, and power

Under a temperature gradient, a thermoelectric voltage V_{th} and current I_{th} are induced in the nanowire device. V_{th} is the electrical potential across the device when the current is zero, i.e. the so-called open-circuit condition, and its proportionality to the temperature difference across the device ΔT is given by the Seebeck coefficient S.

$$V_{\mathrm{th}} = S\Delta T. \tag{2.4}$$

In the linear regime, the I-V relation becomes

$$I(V) = G(V + V_{\mathrm{th}}), \tag{2.5}$$

where G is the conductance of the device. In Paper III, G and S were extracted simultaneously from an *I*-*V* measurement under a known thermal bias ΔT as shown in Fig. 2.6.

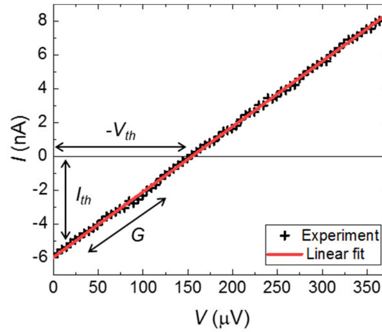

Figure 2.6: Measured $I(V)$ under a thermal bias ΔT. G and S can be extracted simultaneously from the linear fit.

Furthermore, the power dissipated (generated) by the device is given by the product $I \times V$ ($-I \times V$). Finally, the maximum thermoelectric power output $P_{\max}$ of the device is given by

$$P_{\max} = I_{th} V_{th}/4 = S^2 G (\Delta T)^2/4, \quad (2.6)$$

which occurs when the connected external load has the same resistance as the device [17].

2.3.2 Resistance thermometry

The temperature difference ΔT is measured with resistance thermometry. The electrical resistance of metals increases with temperature due to increased electron-electron and electron-phonon scattering rates, therefore it can be used to determine the temperature. However, at low temperatures, except in superconductors, electron-impurity scattering leads to a non-zero resistivity that remains constant or increases (Kondo effect) with decreasing temperatures [4]. In gold, as shown in Fig. 2.7(a), the temperature dependence of the resistivity disappears near 10 K, which limits the temperature range that resistance thermometry can be applied.

The design of the four-probe contact is to enable detection of the local resistance and temperature of the metal close to the nanowire-metal contact. The resistance is extracted by passing a small AC current (~ 20 μA) through the outer pair of probes and measuring the voltage across the inner pair of probes as indicated in Fig. 2.5(c). A Stanford SR830 lock-in amplifier is used for supplying the AC current and lock-in detection of the voltage.

First, the temperature dependence of the resistance is calibrated by changing the temperature of the copper sample holder in the probe station (Fig. 2.7 (a)). Then, the temperatures near the two separate nanowire-metal contacts can be characterized as functions of the heating current I_h. $I_h \sim 10$ mA is typically used in this thesis, which creates a $\Delta T = 5 - 0.5$ K (Fig. 2.7 (b)) depending on the base temperature (10 – 40 K) and the distance between the two 4-probe contacts.

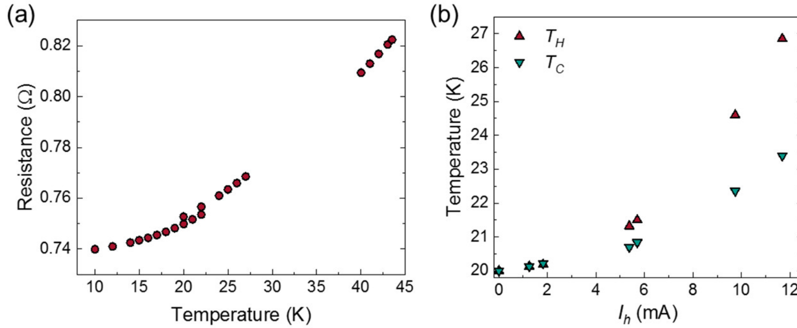

Figure 2.7: (a) Temperature dependent resistance measured by a 4-probe measurement. (b) Temperatures of the two contacts (T_H at the contact close to the heater and T_C at the contact further away from the heater) under application of the heating current I_h at 20 K base temperature.

2.4 Scanning probe thermometry

Due to electrical-thermal energy conversion phenomena such as Joule heating, thermionic emission, and thermoelectric and Peltier effect, electron flows can induce a nonequilibrium temperature distribution. Scanning probe thermometry can resolve the temperature distribution with sub-10 nm resolution [18]. In scanning probe thermometry, a sharp tip is brought into thermal contact with the sample surface. By scanning the tip across the surface, a spatial map of the tip-sample heat transfer is obtained with sensors connected to the tip. The heat flux is determined by both the tip-sample temperature difference and thermal resistance. Therefore, because tip-sample thermal resistance varies significantly with the surface topography of both the sample and the tip, sample temperature cannot be straightforwardly extracted from the measured heat flux [18–20].

In ref. [18,20], the tip is heated by a DC current and the sample temperature is modulated by an AC current. The AC current frequency is sufficiently low so that the sample temperature reaches a steady state. As described in the paragraph below,

through detecting both the DC and AC (through lock-in technique) heat flux, the sample temperature modulation ΔT_{sample} and the tip-sample thermal resistance K_{ts} can be obtained. Here, the scanning probe thermometry setup uses atomic force microscopy as a platform. Thus, the sample temperature and topography are imaged at the same time. The tip-sample distance is detected through the laser beam that is reflected by the cantilever, which is in turn deflected due to the atomic force between the tip and the sample (Fig. 2.8 (a)). The relative position of the sample and the tip are controlled through a closed-loop piezo-scanner[20].

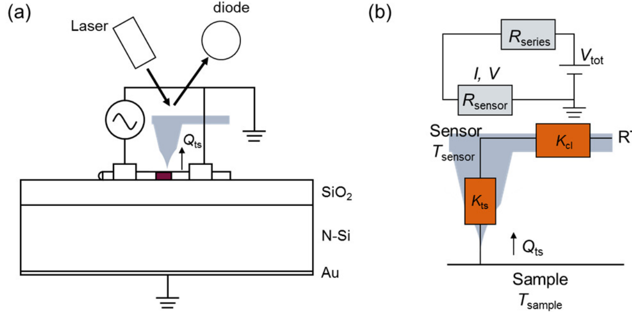

Figure 2.8: (a) Side-view schematics of the device structure and the scanning probe thermal microscopy measurement. (b) The electrical and thermal circuit of the scanning probe.

The cantilever, which is made of highly phosphorus-doped Si, incorporates a region with lower doping that acts as a resistive temperature sensor/heater. The heater and the tip are heated with a constant DC current I, and their temperature can be expressed as

$$T_{sensor} = \mathrm{RT} + \Delta T_{sensor,out}, \tag{2.7}$$

when the tip is *out-of-contact* with the sample. $\Delta T_{sensor,out}$ is related to the heating power IV_{out} and cantilever thermal resistance $K_{cantilever}$ by

$$\Delta T_{sensor,out} = IV_{out} / K_{cl}, \tag{2.8}$$

where $V = V_{out}$ is the voltage at the sensor. The electrical and thermal circuit are shown in Fig. 2.8 (b). When the tip is *in contact* with a sample whose temperature is dynamically modulated with an AC current and expressed as

$$T_{sample} = \mathrm{RT} + \Delta T_{sample,1\omega} (1+ \sin(\omega t)), \tag{2.9}$$

for example, the temperature of the sensor will change accordingly to

$$T_{sensor} = \mathrm{RT} + \Delta T_{sensor,out} + \Delta T_{sensor,DC} + \Delta T_{sensor,1\omega}\sin(\omega t). \tag{2.10}$$

The conservation of energy gives the relation

$$IV_{in} = \frac{T_{sensor}-\mathrm{RT}}{K_{cl}} + \frac{T_{sensor}-T_{sample}}{K_{ts}}, \tag{2.11}$$

where V_{in} is the voltage at the sensor when the tip is *in contact* with the sample and can be expressed as

$$V_{in} = V_{out} + \Delta V_{DC} + \Delta V_{1\omega}\sin(\omega t) \quad . \tag{2.12}$$

In the linear regime, the electrical resistance of the sensor R_{sensor} increases linearly with the temperature as

$$R_{sensor} = R_{sensor,RT}\,(1+\alpha\Delta T_{sensor}). \tag{2.13}$$

Based on Eq. 2.7 - 2.13, $\Delta T_{sample,1\omega}$ and K_{ts} can be extracted from the measured ΔV_{DC}, $\Delta V_{1\omega}$, and $\Delta V_{2\omega}$ with the relation

$$\Delta T_{sample,1\omega} = \Delta T_{sensor,out}\frac{\Delta V_{1\omega}}{\Delta V_{1\omega}-\Delta V_{DC}}. \tag{2.14}$$

2.5 Photocurrent-voltage measurement

In the photocurrent - voltage measurements, the electrical response of the device under the excitation of light is measured. In Papers IV and V, the light source is a supercontinuum laser with a broad spectral width covering 600 – 3000 nm and roughly 400 fs pulse width. A monochromator is used to transmit only light with the selected band of wavelengths.

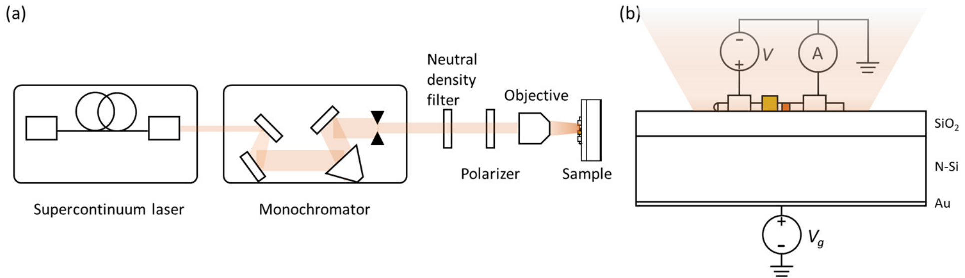

Figure 2.9: (a) Optical devices and components used to control the properties of light. (b) Schematics of the side view of the device structure and the photocurrent-voltage measurement circuitry.

In Paper IV, the electrical measurements are performed in a probe station with a circuitry shown in Fig. 2.9 (b), which allows temperature control between 10 and 300 K, and where the light is transmitted through an optical fiber. In Paper V, the measurement is performed in a table top room temperature setup, which allows the

modulation of light intensity and polarization with a neutral density filter and polarizer, respectively, and the light can be focused onto the device with an objective (Fig. 2.9(a)). The photocurrent is measured by setting $V = 0$, at the so called short-circuit condition. The photovoltages are extracted from I-V measurements similar to thermoelectric voltages in section 2.3.1.

Chapter 3

Electron transport in nanowire polytypic heterostructures

Semiconductor nanowires often contain stacking faults and/or polytype structures, which are crystal structures built by stacking nearly identical atomic layers in different sequences. The electronic properties are influenced by the crystal structures and the mixing of them. This chapter is based on Paper I and II, which are studies on the electronic properties of InAs nanowire zinc blende/ wurtzite heterojunctions.

3.1 Polytypism in semiconductor nanowires

For bulk inorganic semiconductors, the most common crystal structures are zinc blende (ZB) and wurtzite (WZ). For example, bulk nitride-based III-V materials crystalize in hexagonal WZ, while bulk non-nitride III-V and Si crystalize in cubic ZB and diamond structures, respectively[4]. ZB and WZ are crystal polytypes with the same in-plane structure with respect to the most common growth direction <111>. Only their stacking sequence along the growth direction differs, with ABCABC for ZB and ABAB for WZ (Fig. 3.1). The letters A, B, and C refer to a bilayer of group III and V atoms. Higher order polytypes, including 4H (ABCB) and 6H (ABCACB) can also be present[21,22]. Importantly, different crystal phases can coexist in nanowires[8,23].

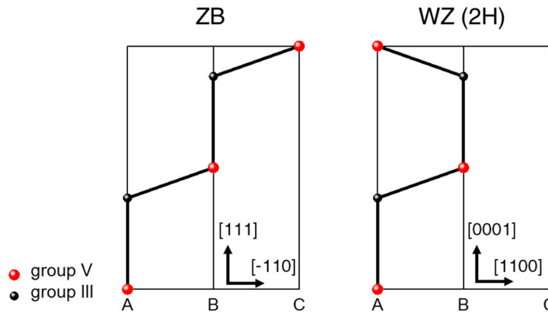

Figure 3.1: Bonding chains of ZB and WZ polytype. The ABC… stacking sequence of ZB and AB… of WZ are shown.

3.2 Band diagram of InAs ZB/WZ heterostructures

For electronic and optoelectronic applications of semiconductor nanowires, it is important to understand how polytypism affects electron transport. Similar to other heterostructures, the electronic transport in polytypic heterostructures can be deduced from the respective electronic properties of the two polytypes, which are influenced by crystal-, interface-, and surface- related effects.

Theoretical calculations have predicted some general trends concerning the electronic properties of bulk non-nitride III-V compounds with ideal ZB and WZ crystal structures. For example, the conduction band minimum of WZ is generally (with few exceptions) higher than that of ZB[24,25]. Furthermore, non-nitride III-V compounds with WZ crystal structures exhibit spontaneous polarizations which are small compared to nitride III-V compounds[26].

In InAs nanowires containing both ZB and WZ crystal phases, electrical characterization on nanowires with native oxide has revealed that WZ segments introduce significant barriers in the conduction band [8,23,27,28]. Below, a description is given on how different effects can lead to conduction band energy barriers in ZB/WZ/ZB InAs nanowires.

3.2.1 Band offset

The electronic band structure is closely linked to the crystal structure. Density functional theory (DFT) calculations have predicted that (at 0 K) WZ InAs has a 36-70 meV larger band gap compared to ZB, and that the WZ conduction band edge is 86-126 meV higher than ZB[24,29,30]. The corresponding conduction band

diagram is shown in the schematics (Fig. 3.2(a), neglecting any other effect at the ZB/WZ interface).

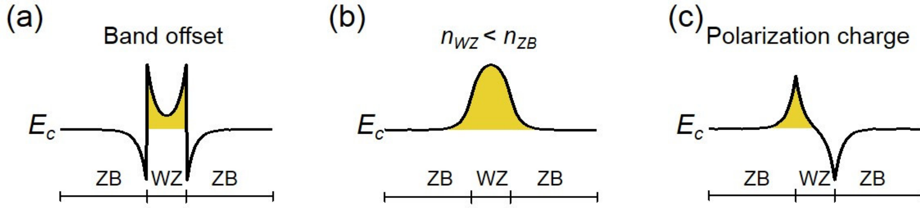

Figure 3.2: Schematics of band diagrams resulting from the individual effect of (a) conduction band offset, (b) carrier concentration difference, and (c) interfacial polarization charge between ZB and WZ.

3.2.2 Carrier concentration difference

InAs with native surface oxides has a high density of donor-type surface states[30], leading to the surface pinning effect with the Fermi level in the conduction band. Therefore, InAs generally has n-type carriers. The density of surface states depends strongly on the oxide species and the nature of the crystal facets[30,31]. Consequently, it is likely that ZB and WZ will have different surface state densities.

Moreover, during nanowire growth using metal-organic precursors, the background carbon can be incorporated into the surfaces of already-grown segments [8,23,32]. Carbon, being an amphoteric dopant in III-Vs, acts as donor in InAs. It is unclear whether carbon incorporation in the ZB and WZ phases occurs in the same manner. Also for crystal structure engineering, ZB and WZ are usually grown at different III/V ratio and/or different temperatures, which will also likely influence carbon incorporation.

In the case where the carrier concentration in WZ is lower than in ZB ($n_{WZ} < n_{ZB}$), the WZ segment included in an otherwise ZB nanowires will create a potential barrier as shown in the conduction band diagram in Fig. 3.2(b) (neglecting any other effect at the ZB/WZ interface).

3.2.3 Polarization effects

In III-V compound, the group III ion cores (e.g. As^{5+}) attract slightly more valence electrons than group V ion cores (e.g. In^{3+})[4], like anions and cations, respectively. Thus the atomic bond is slightly ionic. When the symmetry of the atomic bonds is broken, whether spontaneously or as a result of external fields, polarization fields arise because the centers of the positive and negative charge do not overlap. Under

equilibrium, the atomic bonds form regular tetrahedra in ZB, but are slightly distorted from regular tetrahedra in WZ and lead to spontaneous polarization P_{sp}[26,33]. DFT calculations have found that the atomic bond in the [0001] direction is shortened compared to a regular tetrahedron in non-nitride III-V materials (arsenide, phosphide, and antimonide) and elongated in nitride III-V materials. Correspondingly, DFT shows that P_{sp} are generally positive (pointing in [0001] direction) for non-nitride III-Vs (Fig. 3.3) and negative for nitride III-Vs.

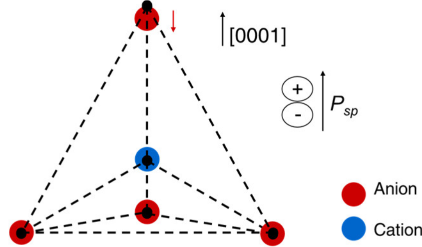

Figure 3.3: Schematics of the WZ crystal structure, in which the atomic bond deviates from a regular tetrahedron (black dashed line). According to DFT simulations, when the bond in the [0001] direction is shortened, a positive P_{sp} is present.

When atomic bonds are altered under strains, an additional polarization, piezoelectric polarization P_{pz} is created. P_{pz} is related to the strain tensor ϵ_j by the piezoelectric tensor e_{ij},

$$P_{pz,i} = \sum_{j=1}^{6} \epsilon_j e_{ij}, \tag{3.1}$$

where Voigt notation is in use with 1 = xx (displacement gradient $\epsilon_{xx} = \frac{\partial u_x}{\partial x}$), 2 = yy, 3 = zz, 4 = yz, 5 = zx, 6 = zy.[34] During epitaxial growth of heterostructures based on two materials with different in-plane lattice constants, an elastic strain and thus a piezoelectric polarization are generated. For nanowires, processing-related strain, such as nanowire bending and strain from the metal contacts, can also induce non-negligible strain and piezoelectric polarization.

The overall lattice (or ionic) contribution to the polarization can be expressed as Eq. 3.2 and is related to the polarization charge density ρ_{pol} by Eq. 3.3. At heterojunctions, an abrupt change in the polarization field leads to a sheet of polarization charges. For a ZB/WZ/ZB structure, polarization charges of opposite signs form at the two opposite interfaces and result in an asymmetric electrostatic field as can be observed in the conduction band diagram schematics (Fig. 3.2(c)).

$$P_{ion} = P_{sp} + P_{pz}. \tag{3.2}$$

$$\rho_{pol} = -\nabla P_{ion}. \tag{3.3}$$

3.3 Semiclassical transport in InAs ZB/WZ heterostructures

In heterostructures, it is important to consider electron transport in each individual material as well as at the heterojunctions. Paper I focuses on electron transport across relatively thick barriers (> 40 nm) at relatively high temperatures (> 100 K). Under this condition, the potential varies slowly compared to the de Broglie wavelength of the electrons, thus the semiclassical model is used to describe the electron motion[35]. In the semiclassical model, electrons are represented by wave packets constructed using energy states in a crystal. They can be treated like classical particles that have well defined positions and momentums, and respond to external fields according to Newton's law. The equations of motion for such electrons under the influence of an electric $\vec{E}$ and magnetic $\vec{H}$ field are

$$\hbar\frac{\partial\vec{k}}{\partial t} = -e\left[\vec{E}(r,t) + \frac{1}{c}\vec{v}(\vec{k}) \times \vec{H}(r,t)\right], \text{ and} \quad (3.4)$$

$$\vec{v}(k) = \frac{\partial E(\vec{k})}{\partial\vec{k}}, \quad (3.5)$$

where $\hbar\vec{k}$ is analogous to the momentum of classical particles, yet the electron velocity $\vec{v}(\vec{k})$ should be inferred from the group velocity of the wave packet [4,35,36].

Based on this picture, electron transport can be calculated from the nonequilibrium distribution of electrons, which can in turn be obtained by solving the Boltzmann transport equation. The simpler drift-diffusion equation derived from the linearized Boltzmann transport equation is commonly used to analyze electron transport in homogeneous semiconductors and semiconductor heterostructures with continuous band structures. However, it cannot be applied in the existence of an abrupt (compared to the relaxation length of electrons) change in band structure. Electron transport at such heterojunctions needs to be considered explicitly, in particular when the electron faces a step-up potential[37]. At high temperatures, electron transport at the interface of an energy barrier occurs predominantly through thermionic emission; but carrier tunnelling is more important for thin barriers and low temperatures.

The current at the heterojunction is considered as a boundary condition that is related to bulk current by the continuity equation[37]

$$\frac{\partial n}{\partial t} = \frac{1}{e}\nabla\cdot J_n + U_n, \quad (3.6)$$

with electron density n, electron current density J_n, and net electron generation rate U_n, which balances the number of electrons. In the steady state, $\frac{\partial n}{\partial t} = 0$ and Eq. 3.6 simplifies to

$$\nabla \cdot J_n = 0, \tag{3.7}$$

when the net carrier generation rate $U_n = 0$.

3.3.1 Boltzmann transport equation and drift-diffusion equation

The average state of electrons in a system can be described by a distribution function $g(r, p, t)$, which gives the probability of finding an electron at time t, located at position r, with momentum p. At thermodynamic equilibrium $g(r, p, t)$ is equivalent to the Fermi-Dirac function f. Under nonequilibrium conditions, electrical conduction can be calculated from $g(r, p, t)$. The (linearized) Boltzmann transport equation

$$\frac{\partial g}{\partial t} + v \cdot \nabla_r g + F \cdot \nabla_p g = \left.\frac{\partial g}{\partial t}\right|_{col} + s(r, p, t) \tag{3.8}$$

then serves as a bookkeeping equation for $g(r, p, t)$ that accounts for any mechanism that might change $g(r, p, t)$, including the net in-flow of electrons into the position $v \cdot \nabla_r g$ or momentum space $F \cdot \nabla_p g$, collision $\left.\frac{\partial g}{\partial t}\right|_{\mathrm{col}}$, and the net electron generation $s(r, p, t)$ as shown in Fig. 3.4.[36] In relaxation time approximation, $\left.\frac{\partial g}{\partial t}\right|_{\mathrm{col}}$ is replaced by $\frac{g}{\tau}$ with the mean electron relaxation time τ.

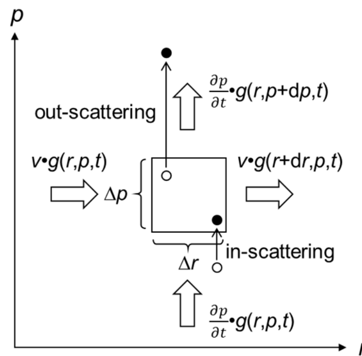

Figure 3.4: Schematics of the bookkeeping characteristics of the Boltzmann transport equation described in Eq. 3.8 [36]

Then, through multiplying the Boltzmann transport equation Eq. 3.8 by the momentum p and sum over the momentum space, the well-known drift-diffusion equation

$$J = e\mu_n nE + eD_n \nabla n, \tag{3.9}$$

with electron mobility $\mu_n = \frac{e\tau}{m^*}$ and diffusivity $D_n = \frac{k_B T}{e}\mu_n$ can be derived.

3.3.2 Thermionic emission

In the thermionic emission theory, carriers with energy greater than the barrier are considered to pass through ballistically, while carriers with energy less than the barrier energy are totally reflected. The overall carrier transport in the heterostructure can be considered as thermionic emission at the heterojunctions in series with drift-diffusion transport in the rest of the transport channel. When the resistances of the rest of the transport channel are relatively small, thermionic emission at the heterojunction is the rate limiting process and the voltage drops primarily at the interface (Fig. 3.5). Under this condition, the electrical current density J can be described by the thermionic emission equation[37–39]

$$J = \frac{4\pi m^* e}{h^3}\int_{V_0}^{\infty} E e^{\frac{-(E-E_f)}{k_B T}}\left[1-\exp\left(-\frac{qV_i}{k_B T}\right)\right]dE = AT^2\exp\left(-\frac{qE_b}{k_B T}\right)\left[1-\exp\left(-\frac{qV_i}{k_B T}\right)\right], \tag{3.10}$$

Where V_0 is the barrier energy relative to the conduction band edge, $E_b = V_0 - E_f$ is the activation energy barrier, V_i is the voltage drop at the heterojunction that electrons are injected, and $A = \frac{4\pi m^* e k_B^2}{h^3}$ is the Richardson constant.

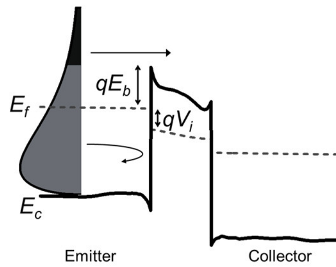

Figure 3.5: Schematics of thermionic emission over an activation energy barrier height E_b.

3.3.3 Extraction of the activation energy barrier

The activation energy barrier height E_b is the energy needed by a carrier at the Fermi level to enter the conduction band of the barrier. When the voltage drop V_i at the heterojunction is larger than $k_B T$, only electrons entering from one side of the barrier are important and the electrical current density can be approximated as $J = AT^2 \exp\left(-\frac{qE_b}{k_B T}\right)$. The temperature dependence of the current can be used to extract the value of E_b.

In Paper I, five sets of InAs nanowires with ZB/WZ/ZB crystal structures, each having an average WZ lengths L_{WZ} = 8, 19, 45, 82, and 210 nm, were investigated experimentally by temperature-dependent electrical characterization. The strong temperature dependence of the current was interpreted as a result of the thermionic emission over the WZ energy barrier. The gate- and bias-voltage dependent activation energy barrier for nanowires with L_{WZ} = 45, 82, and 210 nm can be modelled by numerical simulation (Box 1). Important coefficients such as a ZB/ WZ conduction band offset of 135 ± 10 meV, interfacial polarization charge density on the order of 10^{-3} C/m^2, and carrier concentration an order of magnitude higher in ZB than in WZ, were extracted. Given the small value of the polarization charge, the energy barrier height is mainly determined by the carrier concentration difference and conduction band offset. However, the polarization charge has an important influence on the shape of the barrier.

On the contrary, for $L_{WZ} \leq$ 20 nm, experimentally observed values of the activation energy barrier are significantly lower than the simulated values. This indicates that tunneling transport has become increasingly important.

Box 1 Numerical simulation

For coupled differential equation such as Eq. 3.7 and Eq. 3.9 with boundary condition (Eq. 3.10), analytical solutions do not exist or only exist for some highly symmetric structures. Therefore the next best thing is to search for approximate numerical solutions. In numerical analysis, discretization methods are used to approximate the partial differential equations with numerical model equations, which are then solved with numerical methods. Finite element method in Comsol and Finite difference time domain method in Lumerical (Chapter 5) are used in this thesis to simulate the electronic and optical properties, respectively.

Finite element method (FEM)

The FEM makes use of the weak formulation, or vibrational formulation[40,41]. The weak formulation turns the differential equation into an integral equation. It is called "weak" because it relaxes the requirement in the original PDEs that all the terms must be well defined at all points. The solution to the integral equation in discretized sub-domains then forms the solution of the entire structure.

3.3.4 Thermal-electrical energy conversion in thermionic emission

During the thermionic emission process, carriers with high kinetic energies are injected over the barrier while carriers with low kinetic energies are reflected (Fig. 3.5). This process makes the carrier distributions on both the emitter and collector side out-of-equilibrium with the lattice. On the emitter side, the carriers overall become colder and will absorb heat from the lattice to resume equilibrium, whereas the carriers on the collector side will release heat to the lattice. Thus, thermionic emission can be used as a cooling method.

In analogy to the charge flow expression in Eq. 3.10, the heat flux carried by the thermionic emission current is given as[39]

$$J_Q = \frac{4\pi m^*}{h^3} \int_{E_b}^{\infty} E(E - E_f) e^{\frac{-(E-E_f)}{k_B T}} \left[1 - \exp\left(-\frac{qV_i}{k_B T}\right)\right] dE. \quad (3.11)$$

Overall heat is removed from the emitter side and deposited on the collector side. On each side, the heat will then be exchanged between electrons and the lattice over the energy relaxation length[42].

3.3.5 Scanning probe thermometry

Scanning probe thermometry is used to image the temperature profile of a InAs ZB/WZ/ZB nanowire transistor as studied in Paper I when an AC current $I_{AC} = I_0 \sin(\omega t)$ is applied. The overall temperature modulation of the sample can be expressed as

$$\Delta T(x,y,z,t) = \Delta T_{1\omega}(x,y,z)\sin(\omega t) + \Delta T_{2\omega}(x,y,z)\sin(2\omega t). \quad (3.12)$$

$\Delta T_{1\omega}(x,y,z)$ and $\Delta T_{2\omega}(x,y,z)$ are resolved simultaneously as shown in Fig. 3.6 (b, c).

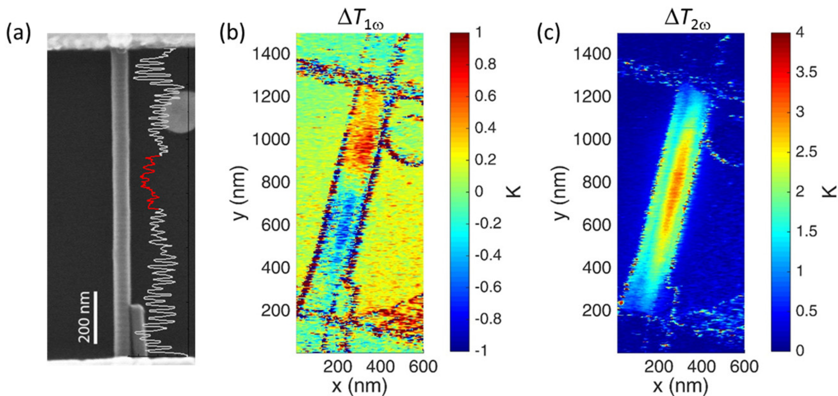

Figure 3.6: (a) InAs ZB/WZ/ZB heterostructure resolved ECCI in SEM. Inset: SEM intensity profile along the nanowire axis where the ZB (gray) and WZ (red) segments

can be distinguished. (b) $\Delta T_{1\omega}$(x,y,z) and (c) $\Delta T_{2\omega}$(x,y,z) measured with the scanning probe thermometry with an AC current around 35 μA at ω ≈ 8 kHz. (b, c) Image credit: Fabian Könemann.

In Fig. 3.6 (b), the $\Delta T_{1\omega}$(x,y,z) data shows that the temperature decreases on one side of the WZ barrier and increases on the other side when an electrical current is passed through the device, which is consistent with the thermionic emission or Peltier effect[18,42]. When the bias is smaller than $k_B T$, the heat flux due to thermionic emission or Peltier effect has a linear dependence on the electric current. Thus, the temperature modulation through Peltier or thermionic effect has an angular frequency 1ω.

In contrast, in Fig. 3.6 (c), the $\Delta T_{2\omega}$(x,y,z) data shows that the temperature increases all over the device, which can be attributed to the Joule heating effect. The electrical energy dissipated in the device is $I^2 R$ with electrical resistance R. Thus the temperature modulation due to Joule heating has an angular frequency 2ω.

3.4 Quantum transport in InAs ZB/WZ heterostructures

Carriers with energies lower than the barriers are allowed to tunnel through them according to quantum mechanics. The tunnelling probability increases as the barrier gets thinner. In Paper I, for $L_{WZ} \leq 20$ nm, the activation energy barrier extracted from the experiment is lower than the simulated value. The deviations are attributed to the increasing importance of the tunnelling current.

When two tunnel barriers are placed close to each other, they form a quantum dot (QD) with discrete electronic states. The energies of these states are determined by Coulomb interaction between the electrons in the QD as well as quantum confinement of the electrons[27,43].

3.4.1 Constant interaction model

The QD is tunnel-coupled to the source/ drain contacts and capacitively coupled to the gate contact as shown in Fig. 3.7(a). In the constant interaction model[44], it is assumed that the total energy of electrons in the QD is given by the sum of the single particle energy ϵ_i plus the electrostatic energy. Thus the energy needed to add N electrons to an empty QD is given as

$$E(N) = \sum_{i=1}^{N} \epsilon_i + \frac{e^2 N^2}{2C_\Sigma} + eN\left(\sum_{j=1}^{m} \frac{C_j}{C_\Sigma} V_j\right), \tag{3.13}$$

where C_j is the capacitance between the QD and the contact j with electrostatic potential V_j and $C_\Sigma = \Sigma C_j$ is the self-capacitance of the QD. By adding one extra charge the electrostatic energy in the QD is changed by the charging energy

$$E_c = \frac{e^2}{C_\Sigma}. \tag{3.14}$$

The energy needed to add the Nth electron can be deduced as

$$\mu_N = E(N) - E(N-1) = \epsilon_N + \frac{e^2}{C_\Sigma}\left(N - \frac{1}{2}\right) + e\left(\sum_{j=1}^{m} \frac{C_{0j}}{C_\Sigma} V_j\right). \tag{3.15}$$

which is $E_c + (\epsilon_N - \epsilon_{N-1})$ higher than the (N-1)th state. The Coulomb charging effect becomes important when E_c is larger than both the energy uncertainty of the electronic state (fulfilled when the QD conductance is lower than conductance quantum e^2/h) and the thermal energy $k_B T$.

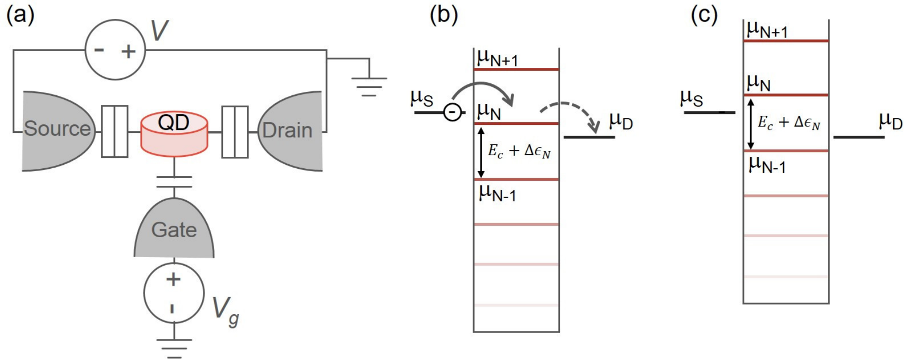

Figure 3.7: (a) Schematics of a QD tunnel coupled to the source/drain contacts and capacitively coupled to the gate contact. (b) The energy diagram of a QD coupled to the source and drain with chemical potential μ_S and μ_D, respectively. Electrons can sequentially tunnel through the QD when there are electronic levels lying within the source-drain bias window. (c) Electron transport is blocked in the Coulomb blockade regime.

In an electrical measurement, the gate voltage can be used to continuously change the electrostatic energy of electrons in the QD. When V_g is tuned so that an electronic state lies between μ_S and μ_D, the electrons can sequentially tunnel in and out of the state and form electrical current (Fig. 3.7(b)). On the contrary, when there is no electronic state between μ_s and μ_d, the transport is blocked (Fig. 3.7(c)), which is referred to as the Coulomb blockade effect. Overall when sweeping V_g at a small constant source drain bias, the current through the QD will show Coulomb oscillations.

The parameters of the QD including E_c, ϵ_i, and the capacitances can be extracted quantitatively by analysing the sizes and shapes of Coulomb diamonds in a charge stability diagram. In such a diagram, the differential conductance dI/dV is plotted as a function of V and V_g. Within the diamond area the conductance is essentially zero due to Coulomb blockade, whereas the blockade is lifted outside the diamond edges.

3.4.2 Quantum dot within an individual WZ barrier

The simulated band diagram of the ZB/WZ/ZB heterostructure shows that due to the conduction band offset, it is possible to form a shallow quantum dot within relatively longer WZ barriers for a small window of Fermi levels (Fig. 3.8(a)).

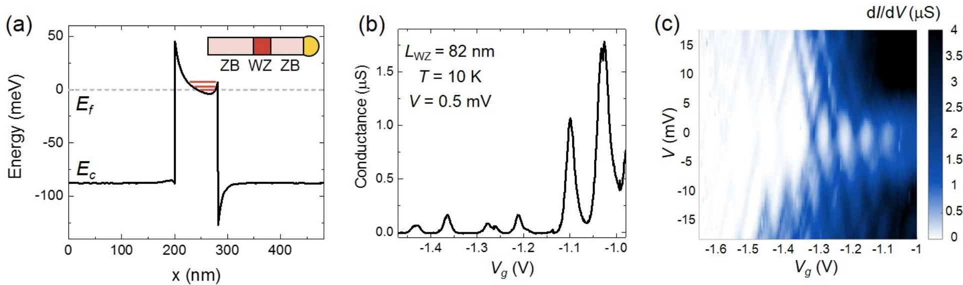

Figure 3.8: (a) The simulated band diagram of ZB/WZ/ZB InAs heterostructure (b, c) Coulomb oscillation and the charge stability diagram showing Coulomb blockade pattern observed experimentally in devices with L_{WZ} = 82 nm.

In Paper I, Coulomb oscillations and Coulomb diamond patterns were repeatedly observed in nanowires with L_{WZ} = 210 and 82 nm in the low temperature (T = 10 K) measurements. The amplitudes of the Coulomb oscillations depend strongly on V_g, as is expected for shallow barriers. In addition, from the Coulomb diamonds, gate capacitances of 2.3 and 4.4 aF are extracted for devices with L_{WZ} = 210 and 82 nm, respectively. The scaling of the gate capacitances with L_{WZ} supports that the QDs were formed within the WZ barrier.

3.4.3 Quantum dot in WZ-ZB-WZ heterostructure

A more reliable way to form QDs is through confinement by two closely spaced WZ barriers. Such QDs have better defined barrier widths and heights.

The quantum confinement is not only affected by the QD geometric structure, but is also influenced by the electrostatic potential landscapes induced by net charges on/within the nanowire and voltages applied on the electrodes. In Paper II,

a pair of side gates are placed next to a QD formed by growth of InAs WZ/ZB/WZ heterostructures (Fig. 3.9(a)). Through tuning the back and side gate potentials, the QD can be split into two smaller QDs. Charge stability diagrams characteristic of parallel-coupled double QDs with varying coupling strengths (from a honeycomb structure to nearly parallel straight lines) were observed in electrical measurements at $T \approx 100$ mK.

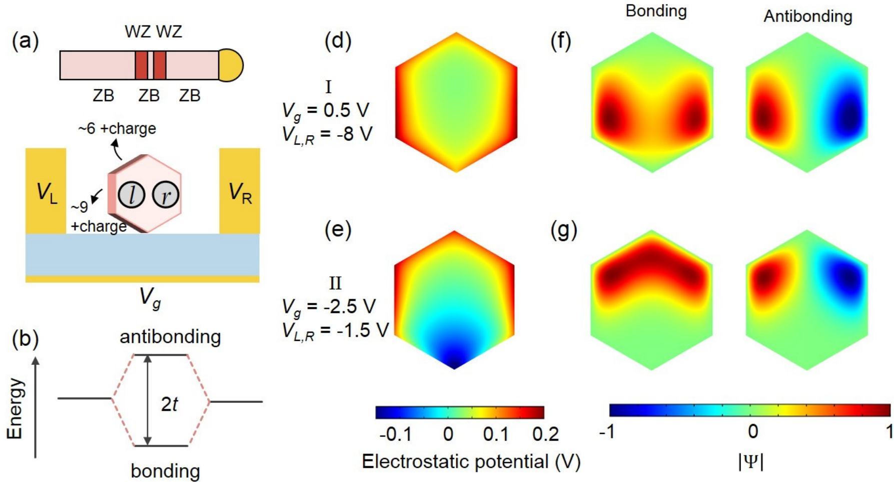

Figure 3.9: (a) Schematics of a QD defined by double WZ barriers in a ZB InAs nanowire. (b) Schematics of the parallel double quantum dots formed through tuning the side gate voltage V_L and V_R and V_g. (d-g) The electrostatic potential and the electronic wave function in the QD under two different gating configurations.

The two QDs can interact through capacitive and tunnel coupling. The experiment shows that different combinations of $V_{L,R}$ and V_g can change the interdot tunnel coupling strength by an order of magnitude.

The interdot tunnel coupling is analogous to molecular bonds. In the strong tunnel coupling regime, electrons can tunnel coherently between the QDs at a large rate[43]. This occurs when the wave functions of the two QDs are delocalized and have significant overlap. The overlapping wave functions then form hybridized states, so-called bonding and antibonding states (Fig. 3.9(b)), over the entire double dot system. The energy difference between the bonding and antibonding state is $2t$, where t is the tunnel coupling strength used in the two-level model to describe double dot interaction.

In Paper II, the finite element method is used to simulate the wave functions and energy of the bonding and antibonding states at different gate configurations. First,

the electrostatic potential $V(x)$ is simulated by solving the Poisson's equation (Eq. (3.1)). Afterwards, the Schrödinger equation

$$-\frac{\hbar^2}{2m}\frac{d^2\psi(x)}{dx^2}+V(x)\psi(x)=E\psi(x), \tag{3.16}$$

at the given $V(x)$ is solved to obtain the electronic state energy E and wave function $\psi(x)$. The solutions correspond to electronic states in an unoccupied QD. To simulate occupied QDs, the Poisson's equation and the Schrödinger equation need to be solved self-consistently.

The simulation results show that it is indeed possible to split one QD into double QDs by controlling the gate voltages. In particular, if considering various positive trapped charges on the side facets (Fig. 3.9(a)) a wide range of gate configurations can lead to the formation of double QD states.

In addition, the simulation results with two different gate configurations (Fig. 3.9 (d-g)) exemplify how different combinations of gate voltages change interdot tunnel coupling. It is clearly visible from the electrostatic potential and the electron wave functions that gate configuration II creates a stronger quantum confinement than gate configuration I. It leads to a stronger the mixing of the wave functions and a larger splitting of the bond and antibond states $2t$ under gate configuration II. The simulated $2t$ are 2.1 meV and 4.8 meV for gate configuration I and II, respectively.

Chapter 4

Thermoelectric effect in 1D nanowires

As a result of the nanowire geometry and the long Fermi wavelength of semiconductors, it is possible to observe (quasi-)1D electronic transport in high crystalline quality semiconductor nanowires at sufficiently low temperatures. 1D electronic transport in thin nanowires has been predicted to give rise to high thermoelectric power factors and energy conversion efficiencies[45,46], which has triggered a widespread effort to develop nanowire-based thermoelectric materials. This chapter introduces Paper III, which reports on an upper limit of the thermoelectric power factor of 1D nanowires, based on theoretical discussions and experimental measurements of InAs nanowires that exhibit quasi-1D electronic transport.

4.1 Thermoelectric effect

The thermoelectric effect refers to that a temperature difference across a material produces electricity, and reversely that an electric current creates a temperature difference across a material. Macroscopic thermoelectric effects were discovered and studied in the 19th century by physicists including Thomas Seebeck, Jean Peltier, and William Thomson[47,48]. The discoveries have led to applications in solid-state power generation, refrigeration, and thermometry. A microscopic understanding only came after the development of quantum mechanics that led to band theory and quantum statistics.

For a material connected to two reservoirs with electrochemical potentials μ_L and μ_R, and temperatures T_L and T_R as illustrated in Fig. 4.1, in the linear regime ($\Delta T = T_L - T_R << (T_L + T_R)/2 = T$ and $eV = \mu_R - \mu_L << k_B T$) the electric current I and heat current I_Q can be described by linear response equations[17,49]

$$I = GV + GS\Delta T, \tag{4.1}$$

$$I_Q = GSTV + (K + GS^2T)\Delta T, \tag{4.2}$$

where G is the electrical conductance, S is the Seebeck coefficient (also called thermopower), and K is the thermal conductance. S and K are defined as the voltage difference and heat flow per temperature difference at the open circuit condition ($I = 0$).

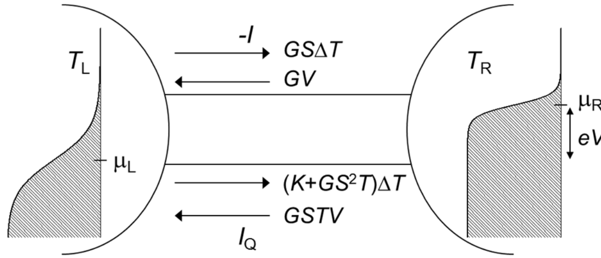

Figure 4.1: Schematic illustration of contributions of each term to the electron and heat flow, $-I$ and I_Q in Eq. 4.1 and 2, between the two reservoirs.

The thermoelectric power output ($= -I\times V$) at a given ΔT reaches a maximum value when $V = S\Delta T/2$ and the maximum power output P_{max} (W) and power output density p_{max} (Wm^{-2}) are given as[17]

$$P_{max} = \frac{1}{4}GS^2\Delta T^2, \text{ and} \tag{4.3}$$

$$p_{max} = \frac{1}{4}\sigma S^2\left(\frac{\partial T}{\partial x}\right)^2 L, \tag{4.4}$$

where L is the distance between the hot and cold reservoir. The products GS^2 and σS^2 are thus known as the *power factors*. In addition, the total energy flow from the right contact to the left contact ($= -I\times V + I_Q$) at $\Delta T = 0$ is maximized when $V = ST/2$ and the maximum energy flow $I_{E,max}$ is given as

$$I_{E,max} = \frac{1}{4}GS^2T^2. \tag{4.5}$$

The energy flow will, however, decrease monotonically as ΔT decreases.

The efficiency of the conversion from heat to work can be expressed as

$$\eta = \frac{-(I\times V)}{I_h}, \tag{4.6}$$

which can be maximized by taking a derivative with V. The maximum efficiency is

$$\eta_{max} = \eta_C \frac{\sqrt{ZT+1}-1}{\sqrt{ZT+1}+1}, \tag{4.7}$$

with the Carnot efficiency $\eta_C = 1 - \frac{T_R}{T_L} \approx \frac{\Delta T}{T}$ in the linear regime, and the figure of merit

$$ZT \equiv \frac{GS^2T}{K}. \tag{4.8}$$

Similarly, the coefficient of performance (COP) of thermoelectric cooling, defined as the heat current extracted from the cold system per electric power input[17], is given as

$$COP = COP_C \frac{\sqrt{ZT+1}+1}{\sqrt{ZT+1}-1}, \tag{4.9}$$

where $COP_C = \frac{T_R}{T_L - T_R} \approx \frac{T}{\Delta T}$ is the limit calculated from a Carnot cycle.

4.2 Size effects in nanowires

In nanostructures, electron transport exhibits different quantum phenomena when the physical dimensions are comparable to (1) the de Broglie wavelength, (2) the mean free path, and (3) the phase relaxation length. These systems are called *mesoscopic* systems[6], as they are in between macroscopic objects and microscopic objects like atoms.

4.2.1 Quantum confinement effect in nanowires

Within the effective mass approximation, the electron wave function in a crystal containing perturbations can be approximated as the product of the wave functions of the perfect crystal and an *envelope function* $\psi(x)$. The Schrödinger equation simplifies to the effective Schrödinger equation for the $\psi(r)$

$$\left[-\frac{\hbar^2}{2m^*}\nabla_r^2 + V_b(r)\right]\psi(r) = E\psi(r), \tag{4.10}$$

with electron effective mass m^* and the energy potential $V_b(r)$[50]. For a perfect infinite crystal, $V_b(r) = 0$ and one possible solution in one-dimension is

$$\psi(x) = e^{ikx}, \tag{4.11}$$

where the wavevector k can take any real value and the electrons are free to move.

However, if the size of the crystal is finite or a quantum well is formed, the motion of the electrons is restricted and the energy levels become discrete. For example, for a crystal extending between $x = 0$ to L, the potential energy can be expressed as

$$\begin{cases} V_b = 0, 0 < x < L \\ V_b = \infty, x < 0, x > L \end{cases} \quad (4.12)$$

and the following boundary conditions apply

$$\begin{cases} \psi(0) = 0 \\ \psi(L) = 0 \end{cases} . \quad (4.13)$$

Thus, the wave functions are

$$\psi_n(x) = \sin(k_n x), \quad (4.14)$$

with discrete wavevectors

$k_n = \frac{n\pi}{L}$, and energies

$$E_n = \frac{\hbar^2 k_n^2}{2m^*}, \quad (4.15)$$

where $n = 1, 2, 3….$

In a nanowire, electrons are constricted in the nanowire cross-section plane, but they can move freely in the axial direction (z-axis). Thus, the 3D envelope function can be expressed as[50,51]

$$\psi(x, y, z) = \varphi(x, y) e^{i k_z z}. \quad (4.16)$$

And the Schrödinger equation becomes

$$\left[-\frac{\hbar^2}{2m^*} \frac{d^2\varphi(x,y)}{dx^2} - \frac{\hbar^2}{2m^*} \frac{d^2\varphi(x,y)}{dy^2} + V(x, y) + \frac{\hbar^2 k_z^2}{2m^*} \right] \varphi(x, y) = E\varphi(x, y) e^{i k_z z}. \quad (4.17)$$

By solving Eq. 4.17, for example for a InAs ($m^* = 0.026\ m_e$[24]) nanowire with 60 nm diameter hexagonal cross-section as studied in paper III, the wave functions in the cross-section plane and the quantized energy levels (E_n) can be obtained (Fig. 4.2(b)).

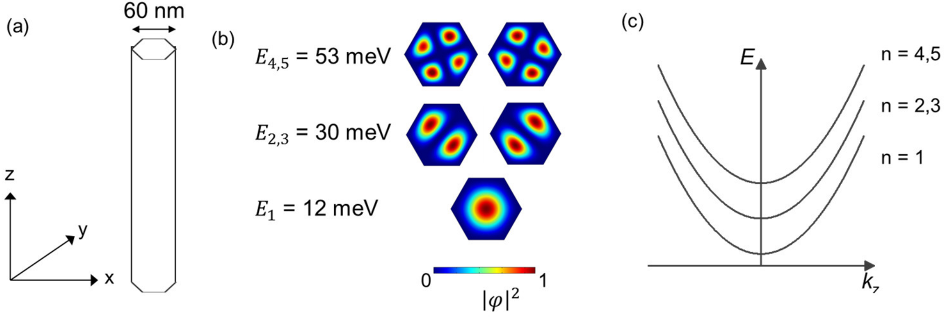

Figure 4.2: (a) Schematics of a nanowire with a 60 nm diameter hexagonal cross-section as studied in Paper III and the corresponding definition of the axis directions used in this section. (b)Wave function intensity $|\varphi|^2$ and quantization energies E_n of the first five electronic states in the nanowire cross-section. (c) The energy dispersion relation of the corresponding quasi-1D states.

Overall, the energy dispersion relation becomes

$$E = E_n + \frac{\hbar^2 k_z^2}{2m^*}, \tag{4.18}$$

as shown in Fig. 4.2 (c). Each parabola is a continuum of one-dimensional states associated with one discrete state (in the cross-section plane). These one-dimensional states are also called 1D subbands, 1D modes, and 1D channels. The quantum confinement effect becomes significant when the quantized energy level spacing is similar to, or larger than, the Fermi energy and thermal energy, which is equivalent to when the nanowire diameter is below or comparable to the electron Fermi wavelength and the thermal de Broglie wavelength.

4.2.2 (Quasi-) ballistic transport and the Landauer formula

In addition to its small cross-section, the length of nanowire devices is also often comparable to other characteristic length scales of electron transport, such as the electron mean free path and the phase relaxation length, which can be as long as several μms in high crystalline quality semiconductors at low temperatures[6,51]. The mean free path is the distance an electron travels before its initial momentum is lost, whereas the phase relaxation length refers to the distance an electron travel before its initial phase is lost.

When the nanowire length is below or similar to the electron mean free path, electrons experience no or few scattering events in the conduction channel; the electron transport is ballistic or quasi-ballistic. Landauer's scattering theory, which describes electron transport properties in terms of the probability that the electrons

go from one reservoir to another[17], is widely used to interpret transport measurements in this regime.

To go from the left to the right reservoir as shown in Fig. 4.3, the electrons will transmit across the reservoir/sample interface, the sample, and the sample/reservoir interface. In the reservoirs, the current is carried by many transverse modes, whereas in a mesoscopic sample there are few modes. Due to current conservation, the total transmission from all the modes in the reservoir (labelled *r*) into a given mode labelled *s* in the sample is [6,17,52]

$$T_s = \sum_r |t_{rs}|^2 \leq 1, \tag{4.19}$$

where t_{rs} is the transmission amplitude from mode *r* to mode *s*. In an ideal contact, where the change from the reservoir to the sample is smooth, $T_s = 1$ and the total transmission at the reservoir/sample interface is proportional to the number of modes $M(E)$ in the sample that are coupled to the reservoir at energy *E*. Conversely, at the sample/reservoir interface, the total transmission is proportional the number of modes in the reservoir at energy *E*, which is extremely large compared to $M(E)$. If we assume the average probability that electrons can be transmitted across the sample is $T(E)$, the charge and heat current from the left to the right reservoir are expressed in Landauer formula as[6]

$$I_{L\to R} = \frac{2e}{h}\int M(E)T(E)f_L(E)dE, \tag{4.20}$$

$$I_{Q,L\to R} = \frac{2}{h}\int (E-\mu)M(E)T(E)f_L(E)dE. \tag{4.21}$$

The prefactor 2 in Eq. 4.20, 21 accounts for the spin degeneracy.

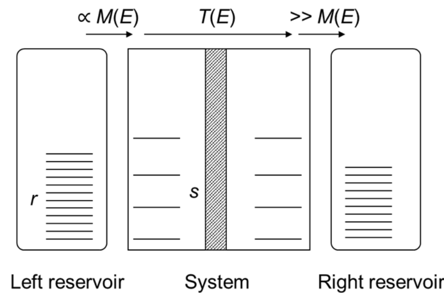

Figure 4.3: Schematic representation of electron transmission from the left reservoir to the right reservoir

Usually the electron phase relaxation length is several times longer than the mean free path in the same sample[51]. The reason is that elastic scatterings (with rigid scatterers, like static impurities and energy barriers) do not contribute to phase relaxation[6,53]. Only inelastic scatterings (with fluctuating scatterers, like lattice

vibrations or electrons) lead to the destruction of phases. Thus, quantum interference can be observed in diffusive samples with dimensions larger than the mean free path.

4.3 Thermoelectric coefficient of quasi-1D systems

Based on the Landauer formula, coefficients that determine the thermoelectric power output/ cooling power, including the conductance and the Seebeck coefficient, can be calculated for a quasi-1D system.

4.3.1 Conductance and Seebeck coefficient

Inferring from Eq. 4.1, 2, 19, 20, the conductance G (= $\frac{\partial I\ (=I_{L\to R}-I_{R\to L})}{\partial V}$) and SG (= $\frac{1}{T}\frac{\partial I_Q\ (=I_{Q,L\to R}-I_{Q,R\to L})}{\partial V}$) can be expressed in linearized equations as[49,50]

$$G = \frac{2e^2}{h}\int M(E)T(E)\frac{-\partial f}{\partial E}dE, \tag{4.22}$$

$$GS = \frac{2e}{hT}\int (E-\mu)M(E)T(E)\frac{-\partial f}{\partial E}dE. \tag{4.23}$$

For an InAs nanowire with geometries illustrated in Fig. 4.2, the number of modes as a function of energy $M(E)$ ($E = 0$ is taken at the conduction band edge of bulk InAs) is shown in Fig. 4.4 (a). The calculated G and S as functions of μ considering ballistic transport ($T(E) = 1$) and $T = 10$ K are shown in Fig. 4.4 (b). It can be observed that each spin degenerate 1D mode can contribute a maximum conductance of $2e^2/h$, which is referred to as the *conductance quantum*.

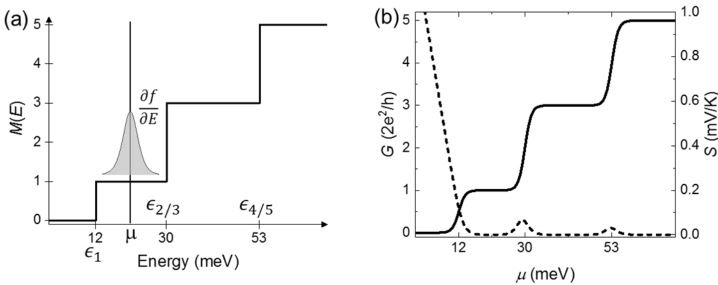

Figure 4.4: (a) Visualization of the number of modes $M(E)$ coupled to the reservoir at energy E for the InAs nanowire with a 60 nm diameter cross-section and $\frac{\partial f(E,\mu)}{\partial E}$. (b) The calculated conductance G and S as functions of μ.

Heisenberg's uncertainty principle, $\Delta E \Delta t \geq h$, provides another way to obtain the conductance quantum. The current can be expressed as $I = e/\Delta t$, where Δt is the time it takes a charge to traverse the system. In the meantime, the bias gives the uncertainty in energy ΔE = eV. Therefore the uncertainty principles gives that $G = \frac{e^2}{\Delta E \Delta t} \leq \frac{e^2}{h}$[54,55].

It can be inferred from Eq. 4.23 that S is non-zero whenever the dynamics of electrons with energy above μ are different than the dynamics of electrons with energy below μ. Thus, for a ballistic quasi-1D system, S is zero except when $|\mu - E_n|$ is below or comparable to $k_B T$ or $\mu < E_1$.

4.3.2 Power factor limit of a 1D channel

From Eq. 4.22 and 23, the power factor S^2G can also be calculated. In ref.[56,57], only one 1D mode is considered and it is found that the thermoelectric power output is maximized when $T(E)$ is a Heaviside step function. The maximum power output for a 1D mode, referred to as the quantum bound, is $P_{QB} = A_0 \pi^2 k^2 \Delta T^2/h$ with $A_0 \approx 0.0321$. Thus from Eq. 4.3, it is equivalent to saying that the quantum bound of the power factor for a spin-degenerate 1D mode is

$$(S^2G)_{QB} = 2 \times 4A_0 \frac{\pi^2}{h} k_B^2 \approx 0.73 \text{ (pW/K}^2\text{)}. \quad (4.24)$$

The step transmission function is fulfilled in ballistic 1D channels, thus S^2G calculated for the ballistic quasi-1D system shows a maximum $S^2G \approx (S^2G)_{QB}$ for $E_2 - E_1 >> k_B T$ (Fig. 4.5). However, S^2G of a quasi-1D system can potentially exceed $(S^2G)_{QB}$ when $E_2 - E_1$ is below or similar to $k_B T$ and electrons are conducted through multiple 1D modes.

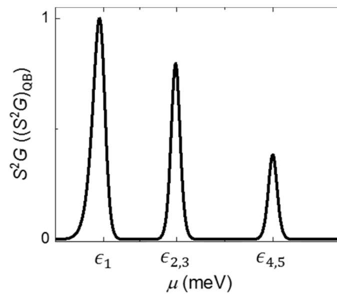

Figure 4.5: The calculated power factor S^2G of an InAs nanowire with a 60 nm diameter cross-section.

Paper III extends the results in ref.[56,57] to find the power factor upper limit for a non-ballistic 1D channel, i.e. when $T(E)$ is less than unity. Consider a realistic

1D channel with transmission probability $t(E)$ shown in Fig. 4.6, which can be expressed as

$$t(E) = T_{\max}\phi(E), \quad (4.25)$$

where $T_{\max}$ describes the maximum height of $t(E)$, and $\phi(E)$ is a normalized function that describes the shape of $t(E)$. S^2G calculated from $t(E)$ is necessarily less than or equal to S^2G calculated from a virtual transmission function $T_{\max}\theta(E)$, where $\theta(E)$ is a Heaviside step function. Thus by inserting $T_{\max}\theta(E)$ into Eq. 4.22, 23, a power factor limit

$$(S^2G)_{\text{limit}} = T_{\max}\times(S^2G)_{\text{QB}} \quad (4.26)$$

is obtained. The increasing trend of $(S^2G)_{\text{limit}}$ with $T_{\max}$ is consistent with experimental results in Paper III.

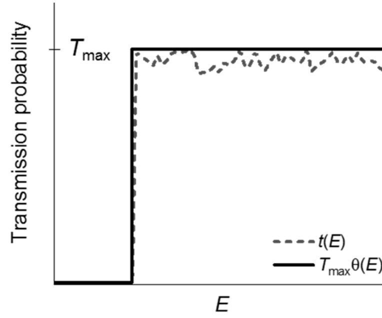

Figure 4.6: The transmission probability $t(E) = T_{\max}\phi(E)$ of a hypothetical 1D channel and a step function with the same height $T_{\max}\theta(E)$.

$(S^2G)_{\text{limit}}$ can be further extended to the limit of $S^2\sigma$ if a classical scaling of the transmission probability[58]

$$T = \frac{\Lambda}{L+\Lambda}, \quad (4.27)$$

with the channel length L is considered. Λ is a constant on the order of the mean free path that represents the channel length when the transmission probability is 0.5. A detailed explanation of this scaling relation is given in Box 2 below. Combining Eq. 4.25, 26, the upper limit of $S^2\sigma$ can be expressed as

$$(S^2\sigma)_{\text{limit}} = (S^2G)_{\text{limit}} \times \frac{L}{A} \leq (S^2G)_{QB} \times \frac{\Lambda}{A}, \quad (4.28)$$

with nanowire cross-section area A. The expression of $(S^2\sigma)_{\text{limit}}$ highlights one of the most important advantages of using nanowires as thermoelectric materials: the thermoelectric power output density can be increased simply through reducing the nanowire diameter.

Box 2 Classical transmission probability

In the non-ballistic transport regime, if all the quantum interference effects are neglected, the total transmission probability of successive scattering sections labelled 1 and 2 in Fig. B2.1 can be written as[7,58]

$T_{12} = T_1T_2(1 + R_1R_2 + (R_1R_2)^2 + \cdots) = \frac{T_1T_2}{T_1+T_2-T_1T_2}$, and that

$\frac{1}{T_{12}} = \frac{1}{T_1} + \frac{1}{T_2} - 1.$

Thus, Eq. 4.27 is obtained by finding an expression that satisfies

$\frac{1}{T(L_1+L_2)} = \frac{1}{T(L_1)} + \frac{1}{T(L_2)} - 1.$

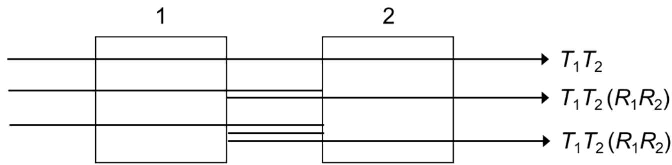

Figure B2.1: Schematic representations of different transmission paths through two successive scattering sections.

Chapter 5

Photo-excited hot-carrier effect in nanowire heterostructures

The unique optical, electronic, and material properties make semiconductor nanowires promising candidates for realizing optical hot-carrier devices. In this chapter different aspects of such devices, including nanophotonic effects and the collection of nonequilibrium carriers, are discussed.

5.1 Hot-carrier based optoelectronic devices

The term “hot carrier” broadly refers to electric charge carriers (i.e. electrons in metals, and electrons and holes in semiconductors) that have gained excess kinetic energy due to external perturbations like electric fields or optical excitations and have a nonequilibrium distribution[59]. In conventional p-n junction photovoltaic solar cells, the photo-excited electrons and holes have lost most of their excess energy and have relaxed to near the band edge before being collected to different sides of the diode[60]. The thermal relaxation of the carriers and the transmission of photons with energy below the bandgap are the most important fundamental loss mechanisms in conventional solar cells[61,62].

For these reasons, hot-carrier solar cells are designed to collect the photo-excited carriers before they fully relax to near the band edge. Thermodynamic analysis has shown that more power can be extracted from carriers that have a higher temperature than the collector[63–65]. Many device concepts have been proposed and tested; these devices generally use energy barriers to extract hot-carriers with different

nonequilibrium characteristics that can be categorized into thermal and non-thermal distributions, which are generated through plasmon decay in metals and direct photo-excitation in both metals and semiconductors [66–70].

In photodetectors including photoconductors, p-i-n photodiodes, and Schottky photodiodes (operated with electrons-holes generated in the semiconductor), the photo-excited carriers have relaxed to near the band edge as they transport across the absorption region. Therefore, the photocurrent signal recovery time can last as long as the carrier recombination lifetime [71] and limit their application in high-speed photodetection [72]. From this perspective, hot-carrier photodetectors based on internal photoemission in Schottky diodes (operated with electrons generated in the metal) [73–75] have a significant advantage because the thermalized carriers are blocked off by the Schottky barrier and the signal recovery time is thus only limited by the much more rapid carrier thermal relaxation [66,76]. However, the photodetection speed is also limited by factors including the carrier transit time, RC time constant, carrier trapping, and the connection to external circuits [71].

Despite these advantages, hot-carrier solar cells and photodetectors still face the challenge of low internal quantum efficiency [70,74,77,78]. Thus more understanding of hot-carrier transport and new device schemes are desired. Paper V demonstrates a nanowire-metal plasmonic antenna hybrid device, as shown in Fig. 5.1. In these devices, optical absorption is enhanced due to the plasmonic effect. In addition, the position and the energy of the generated hot-electrons can be controlled by the position of the plasmonic antenna (the electric field is concentrated in the gap of the antenna dipole [79,80]) and the energy of the incident photons, respectively, which permits a detailed study of their transport.

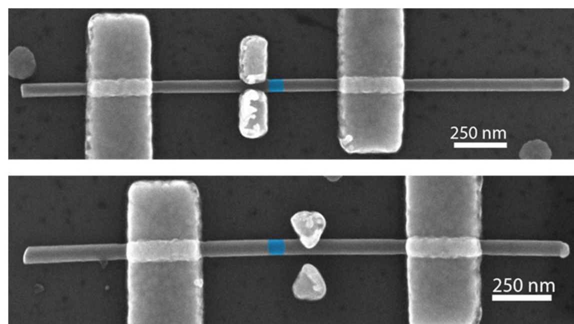

Figure 5.1: SEM images of InAs-InP-InAs nanowire-metal plasmonic antenna hybrid devices. The InP segments are false colored in blue.

5.2 Optical effects in nanowire-based structures

The dimensions of the semiconductor nanowire and the metal nanostructures in single-nanowire devices are comparable to the wavelength of light. Therefore, they can be designed to exhibit unique optical responses, such as enhanced absorption, based on different light resonances. These effects can be understood based on Maxwell's equations and the optical properties of the constituent media.

In a medium, a polarization P and a current J can be induced in response to an electric field $\vec{E}$. If the medium is linear and isotropic, their relation can be described by the equations [50,81]

$$\vec{D} = \varepsilon_0\vec{E} + \vec{P} = \varepsilon_r\varepsilon_0\vec{E}, \tag{5.1}$$

$$J = \sigma\vec{E}, \tag{5.2}$$

with the electric displacement field $\vec{D}$, vacuum permittivity ε_0, dielectric function ε_r, and conductivity σ. For a single Fourier component of the electric field $E(\omega)\exp(ikr - \omega t)$, with wavevector k and angular frequency ω, the Maxwell–Ampère equation is [50,81]

$$\nabla \times H(\omega) = J(\omega) + \frac{\partial D(\omega)}{\partial t} = \sigma(\omega)E(\omega) - i\omega\varepsilon_0\varepsilon_r E(\omega) = -i\omega\varepsilon_0\widetilde{\varepsilon_r}E(\omega). \tag{5.3}$$

The complex dielectric function $\tilde{\varepsilon}$ (ω) expressed as

$$\tilde{\varepsilon}(\omega) = \varepsilon_r(\omega) + \frac{i\sigma(\omega)}{\omega\varepsilon_0} = \varepsilon_1 + i\varepsilon_2 \tag{5.4}$$

thus contains both the conduction and the polarization response to an oscillating electric field. The complex refractive index $\tilde{n}(\omega) = n(\omega) + i\kappa(\omega)$ with the refractive index $n(\omega)$ and the extinction coefficient $\kappa(\omega)$ are given as $\tilde{n}(\omega)^2 = \tilde{\varepsilon}(\omega)$, thus

$$n(\omega)^2 = \frac{\varepsilon_1}{2} + \frac{1}{2}\sqrt{\varepsilon_1^2 + \varepsilon_2^2}, \text{ and} \tag{5.5}$$

$$\kappa(\omega) = \frac{\varepsilon_2}{2n}, \tag{5.6}$$

which is in turn connected to the absorption coefficient $\alpha(\omega)$ by

$$\alpha(\omega) = \frac{2\kappa(\omega)\omega}{c}. \tag{5.7}$$

In metals, the dielectric function is dominated by the conduction of free electrons. The interaction of the free electrons with light can be understood based on the classical equation of motion, which is described in the Drude model. The natural resonant frequency of the collective movement of the free electrons called the *plasma frequency* ω_p with

$$\omega_p^2 = \frac{4ne^2}{\varepsilon_0 m^*}, \tag{5.8}$$

can be derived from the model [81]. ω_p of metals is usually in the deep UV range, for example ω_p is around 9 eV for gold [82]. When the incoming light has frequency $\omega < \omega_p$, the free electrons have a large in-phase movement, creating a large negative polarization. Thus Re $[\tilde{\varepsilon}(\omega)]$ of metals are characterized by large negative values (Fig. 5.2(a)).

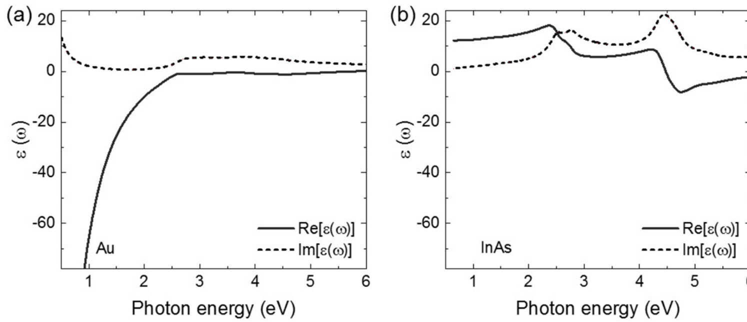

Figure 5.2: The complex dielectric function of (a) Au [83] and (b) InAs [84].

In semiconductors, the density of free carriers is much lower and the plasma frequency is usually in the THz range. Therefore, in the visible to infrared range, the dielectric function is dominated by the atomic polarizability and interband transition of electrons. The atomic polarization arises from the motion of electrons that are bound to the ion core [4,85] and it gives a large positive Re $[\varepsilon(\omega)]$ in the visible to infrared range in semiconductors. However when strong interband transition occurs at higher photon energy, it will also induce a negative Re $[\tilde{\varepsilon}(\omega)]$ (Fig. 5.2(b)).

5.2.1 Optical resonances in nanowires

Given the large positive Re $[\varepsilon(\omega)]$ and $n(\omega)$, strong optical resonance modes can exist in single nanowires with subwavelength dimensions and in nanowire arrays. For light incident perpendicular to the axis of a single nanowire, the interference of light reflected at the boundary leads to optical resonance modes. Such a resonance is often called the leaky mode resonance because a significant part of the field resides outside of the nanowire [11,86].

By approximating the nanowire to an infinitely long cylinder, the Lorenz-Mie theory provides analytic solutions to Maxwell's equations [10,11]. Thus, the scattering and absorption of electromagnetic waves by objects with dimensions smaller than the wavelengths with either spherical or infinite cylindrical geometries can be calculated. In Fig. 5.3, the calculated absorption efficiency, defined as the absorbed power/ (incident irradiance (Wm^{-2}) $\times$ particle cross-sectional area

projected onto the plane perpendicular to the incident direction (m^2)), of a cylindrical InAs nanowire with 60 nm diameter is shown. The incident light is perpendicular to the nanowire axis with transverse-magnetic (TM, electric field // nanowire axis) and transverse-electric (TE, electric field ⊥ nanowire axis) polarization. A light concentration effect can be observed around the resonant energies.

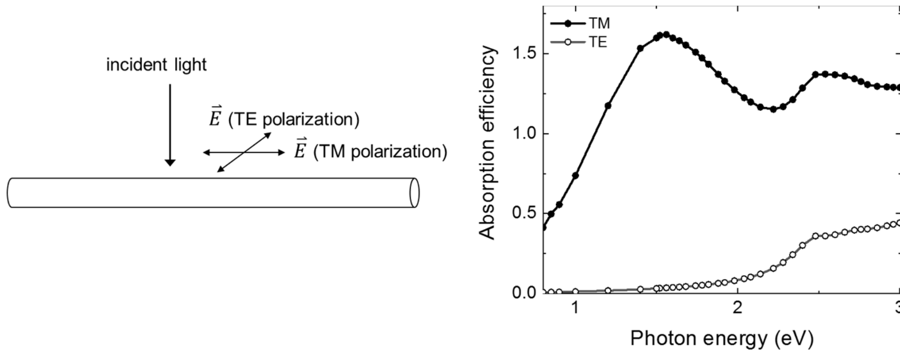

Figure 5.3: The absorption efficiency of an infinitely long cylindrical InAs nanowire with 60 nm diameter calculated based on the Lorenz-Mie theory. The light is incident perpendicular to the nanowire axis with electric field perpendicular (TE) and parallel (TM) to the nanowire axis.

5.2.2 Plasmonic effect

In metals, the large negative Re [$\tilde{\varepsilon}(\omega)$] leads to a surface plasmon polariton mode at metal-dielectric interfaces, and localized surface plasmon resonances in metal nanostructures [81]. In these excitations, the electromagnetic fields are coupled with the oscillations of the conduction electron. The surface plasmon polaritons are propagating waves that need to be excited through techniques that fulfill phase-matching. The localized surface plasmons are non-propagating excitations that can be excited through direct illumination. Both types of resonances can achieve concentration of electromagnetic energy below the diffraction limit. Therefore, metal nanostructures can be used as optical antennas to convert freely propagating visible and infrared radiations into localized energy [79,80,87].

The localized plasmon resonance can be understood by considering the interaction of a metal particle with an electromagnetic wave. When the size of the metal particle is much smaller than the wavelength of the incident electromagnetic wave, their interaction can be analyzed by approximating the electromagnetic wave as a static electric field. Then the electric field near the metal particle can be obtained through solving the Laplace equation for the electrostatic potential V, $\nabla^2 V = 0$ with the continuous boundary conditions for the electric field[81]. For a spherical metal

nanoparticle (with complex dielectric function $\tilde{\varepsilon}(\omega)$ and radius a) surrounded by an isotropic dielectric material (with dielectric functionε_d), an electric field $\vec{E}_0$ induces a dipole moment [81]

$$\vec{p} = 4\pi\varepsilon_0\varepsilon_d a^3 \frac{\tilde{\varepsilon}(\omega)-\varepsilon_d}{\tilde{\varepsilon}(\omega)+2\varepsilon_d}\vec{E}_0, \quad (5.9)$$

in the metal sphere, which results in electric fields inside and outside of the metal expressed as

$$\vec{E}_{in} = \frac{3\varepsilon_d}{\tilde{\varepsilon}(\omega)+2\varepsilon_d}\vec{E}_0 \text{ and } \vec{E}_{out} = \vec{E}_0 \frac{3\vec{n}(\vec{n}\cdot\vec{p})-\vec{p}}{4\pi\varepsilon_0\varepsilon_d}\frac{1}{r^3}, \quad (5.10)$$

respectively. The electric near fields are resonantly enhanced and the localized plasmon resonance occurs when the Fröhlich condition Re $[\tilde{\varepsilon}(\omega)] = -2\varepsilon_d$ is satisfied. The finite-difference time-domain method (FDTD, Box 3) is often used to model the spectral response and the near field distribution of optical and plasmonic resonances. Fig. 5.4(a) shows the simulated electric field near a gold sphere with 50 nm diameter surrounded by vacuum and illuminated with a plane wave, which is linearly polarized in the x direction and has a 1000 nm wavelength. A field enhancement can be observed near the gold sphere – vacuum interface (indicated with a white dashed line).

When the nanoparticles are larger, the phase change of the incident electromagnetic field over the nanoparticle volume is non-negligible, and an electrodynamic approach is required to calculate the localized plasmon resonances. In this regime, the resonant frequency can be controlled by changing the particle sizes and shapes.

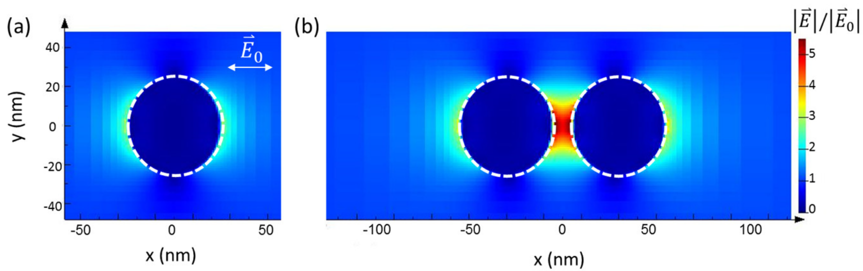

Figure 5.4: FDTD simulation of the electric field amplitude distribution for (a) a gold sphere with a 50 nm diameter and (b) two gold spheres with 50 nm diameters separated by 10 nm surrounded by vacuum and illuminated with a plane wave polarized in the xi direction with 1000 nm wavelength. The boundary of the spheres are indicated by white dashed lines.

Moreover, when a pair of nanoparticles are placed closely to each other, an even stronger near field enhancements can be induced in the gap due to the Coulomb interaction between them as shown in the FDTD simulation results for two gold spheres separated by a 10 nm gap in Fig. 5.4 (b) [81]. For inter-particle spacing much smaller than the wavelength, the two nanoparticles act as a nanocapacitor, therefore their interaction and thus the field enhancement strongly depend on the spacing [79,80].

Box 3 Finite-difference time-domain method (FDTD)

The FDTD is used for modelling electromagnetic waves interacting with material structures. In FDTD, a finite-difference approximation is applied to the time and space derivatives of each electric (*E*) and magnetic (*H*) vector components in Maxwell's equation. The time and space are discretized in a way that *E* and *H* are shifted by half of the discretization in both space and time[40,88].

Then the resulting finite-difference equations are solved. First *H* is solved in a certain spatial location at a given instant in time. Then *E* is solved at one time-step into the future based on the past fields, and the process is iterated until the desired transient or steady-state electromagnetic field behaviour is fully evolved. Because FDTD is a time-domain method, a single simulation can cover a wide spectral range.

5.2.3 Optical absorption

The absorption of electromagnetic radiation in a medium is characterized by the absorption coefficient $\alpha(\omega)$, which is defined as the fraction of power absorbed in a unit length and can be expressed as[89,90]

$$\frac{dI}{dz} = -\alpha(\omega)I, \quad (5.11)$$

where $I = |\vec{E}|^2$ is the intensity and z is the propagation axis of the electromagnetic wave. $\alpha(\omega)$ can be calculated using perturbation theory. Under the perturbation of the electric field $\vec{e}E_0(\omega)\exp(ikr - \omega t)$, the electron transition rate from state i to state j is given by Fermi's golden rule as[50]

$$W_{i,j} = \frac{2\pi}{\hbar}\left(\frac{eE_0}{m_0\omega}\right)^2 |\langle j|\vec{e}\cdot\hat{p}|i\rangle|^2 \delta(E_j - E_i - \hbar\omega), \quad (5.12)$$

where $\hat{p} = -i\hbar\nabla$ is the momentum operator. The energy and momentum must be conserved for the transition with

$$E_j = E_i + \hbar\omega \text{ and } \hbar q_j = \hbar q_i + \hbar k \approx \hbar q_i, \quad (5.13)$$

where $\hbar q_j$, $\hbar q_i$, and $\hbar k$ are the momentum of the final state, the initial state, and the photon. The photon however carries relatively little momentum, therefore the conservation condition is simplified to $E_j(q_i) = E_i(q_i) + \hbar\omega$ in Eq. 5.12.

In semiconductors, electrons in the valence band can transition to the conduction band through absorbing a photon as shown in Fig. 5.5, which is referred to as the interband absorption. In this process, a mobile electron and hole are created in the conduction and valence band, respectively. The energy of the initial and final states must follow

$$\hbar\omega = E_c(q) - E_v(q), \tag{5.14}$$

where $E_c(q)$ and $E_v(q)$ are the energy of the conduction and the valence band at crystal momentum q. In a semiconductor with a direct band gap E_g, by approximating the band structures as parabolas with effective mass m_c and m_v, respectively, the energies of the electron and hole can be calculated from $\hbar\omega = E_g + (\hbar^2q^2/2m_c) + (\hbar^2q^2/2m_v)$. Another type of absorption, intraband absorption, is also possible in semiconductors as shown in Fig. 5.5. However, scattering with, for example, phonons or impurities is needed to achieve the conservation of the momentum[91].

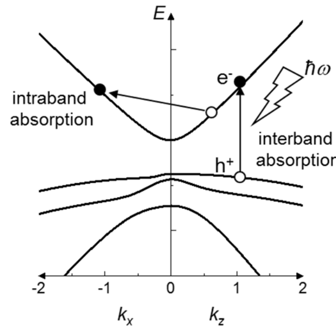

Figure 5.5: Schematics of the electronic band structure and the electron transition during interband and intraband absorption.

Finally, the overall absorption coefficient is obtained by summing over all possible initial and final states[50]

$$\alpha(\omega) = \frac{2\pi e^2}{m^2\omega\varepsilon_0 nc}\left(\frac{E_0}{\omega}\right)^2 \sum_{i,j} |\langle j|\vec{e}\cdot\hat{p}|i\rangle|^2 \delta\left(E_j - E_i - \hbar\omega\right)[f(E_i) - f(E_j)], \tag{5.15}$$

where f is the Fermi-Dirac distribution.

5.3 Photo-excited carrier dynamics

The absorption of photons leads to a nonequilibrium distribution of electrons and holes. In particular, the electrons and holes created through absorbing high energy photons ($\hbar\omega >> E_g$) will have much higher kinetic energies compared to the background electrons (Fig. 5.6 (b)) and the lattice. In addition, the photo-excited electrons and holes can also have an anisotropic momentum distribution[92].

The dynamics of the electrons and holes are best observed when the photoexcitation is achieved by an ultrashort pulse. After the photoexcitation, the perturbed electrons and holes will eventually relax to a thermodynamic equilibrium state through different scattering processes, which take place at different rates. Typically electron-electron and hole-hole scattering have a characteristic time scale from a few fs to hundreds of fs[92,93]. The scattering leads to momentum and energy exchange between the electrons (holes), which result in a more isotropic carrier distribution and brings the electrons (holes) into hot thermalized distributions (follow the Fermi-Dirac statistics) as shown in Fig. 5.6 (c). The difference between the masses of electrons and holes reduces the energy exchange between the two types of carriers. Next, electron-phonon scattering, which, according to Monte Carlo simulations[94,95], has a characteristic time from a few fs to a few hundreds of fs depending on the electron energy in InAs, will cool down the hot electrons to a common temperature with the lattice (Fig. 5.6 (d)). Finally, the excess electrons and holes recombine, which has a characteristic time up to ns in InAs thin films[96], and the system will reach thermodynamic equilibrium .

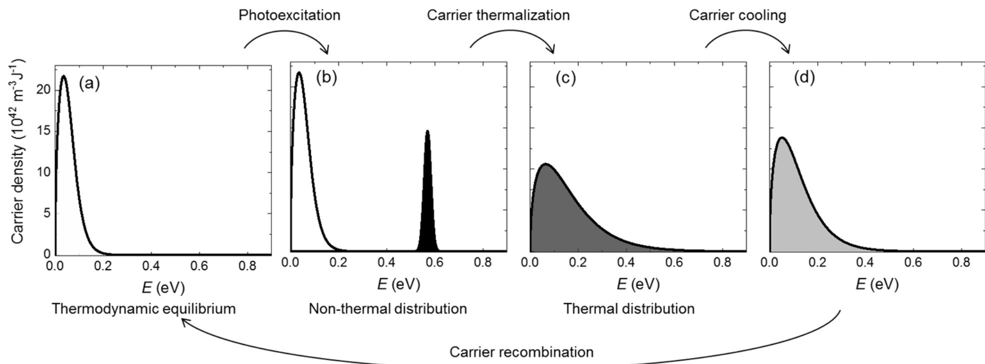

Figure 5.6: The energy distribution of electrons in the conduction band when (a) the system is in thermodynamic equilibrium, (b) electrons are generated through the interband absorption of an ultrashort pulse of monochromatic light, (c) the photo-excited electrons and the background electrons are thermalized, and (d) the thermalized hot-electrons are cooled down by transferring energy to the lattice.

5.4 Photo-excited carrier transport

A photocurrent can be generated by extracting the photo-excited carriers at different time scales, at which the carriers have different nonequilibrium distributions, through different transport mechanisms. In particular, the distribution of the photo-excited carriers can be categorized into two cases: non-thermal and thermal. Energy barriers or energy selective contacts are usually used to extract the photo-excited electrons and holes into separate electrodes. In Paper IV and V, the energy barrier formed by InP is used to extract hot electrons generated in InAs and forbid the backflow of low energy electrons, while reflecting the simultaneously generated holes that are much less energetic due to the large hole effective mass.

The photocurrent arising from non-thermal hot-carriers can be modelled based on the energy distribution of the carriers and the internal photoemission transport models. For thermalized hot-carriers, the thermionic emission model can be used [66,97,98].

5.4.1 Internal photoemission effect

Internal photoemission is the process of electrons being emitted from one material to another after the absorption of photons. The process can be separated into a sequence of relatively independent steps[78,98], which, in the following, will be described based on the WZ InAs/InP/InAs heterostructure studied in Paper V with band alignment illustrated in Fig. 5.7(a)[24].

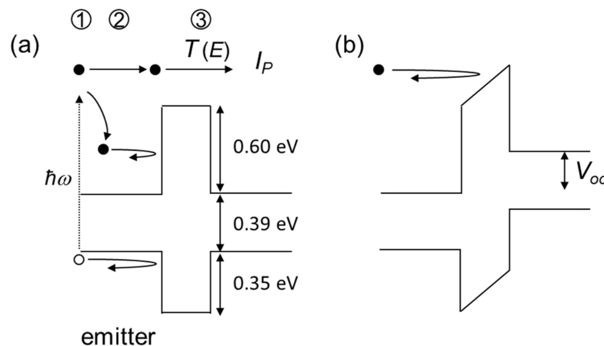

Figure 5.7: (a) Band diagram of the WZ InAs/InP/InAs heterostructure. The arrows indicate the sequential steps of internal photoemission: (1) electrons/holes are created in the emitter through interband absorption, (2) electrons/holes transport toward the InAs/InP interface and carrier relaxation can simultaneously occur, and (3) energetic electrons transmit through the barrier and form the photocurrent I_P. (b) When a bias is applied to the device, the barrier height is increased, which allows to extract the open circuit voltage V_{OC}.

First, energetic mobile electrons and less energetic holes are created in the emitter through absorbing photons with energy $\hbar\omega$ larger than the band gap E_g. Based on the parabolic effective mass approximation, in InAs (with electron and hole effective mass $m_{e,InAs} = 0.026\ m_e$, $m_{h,InAs} = 0.625\ m_e$), electrons carry most of the photon energy in excess of the band gap, $\frac{m_{h,InAs}}{m_{e,InAs}+m_{h,InAs}}(\hbar\omega - E_g)$. A more accurate energy distribution of the photo-excited electrons and holes can be deduced from the complete band structure based on energy and momentum conservation as described in Eq. 5.14.

Afterwards, on average, half of the photo-excited electrons (and holes) transport towards the InAs/InP interface. During the transport, the momentum of the electrons can be redirected due to elastic scattering; and the energy distribution of the electrons can be changed due to inelastic scattering[98].

Finally, the photocurrent I_P can be calculated by the integral

$$I_P(\hbar\omega) = e\int n(E,\hbar\omega)\bar{T}(E)\,dE, \qquad (5.16)$$

where $n(E, \hbar\omega)$ is the energy distribution of electron flux at the InAs/InP interface and $\bar{T}(E)$ is the barrier transmission probability. The semiclassical transmission model is usually used for Schottky barriers, which are non-rectangular [37,39,99]. However, for rectangular barriers induced by band offsets in semiconductor heterostructure, quantum interference between the incident and reflected electron waves becomes more important[50,51] and the quantum mechanical transmission model[50,100] can be used (Box 4).

Box 4 Barrier transmission probability

Quantum mechanical transmission model

When an electron traveling in the $+z$ direction with kinetic energy E_z encounters a potential barrier, its transmission and reflection probability can be obtained by solving the 1D Schrödinger equation for the envelope function. If the electron transport is **coherent** across the barrier, for a potential step shown in Fig. B4.1(a), the time-independent wave function takes the form[50,100]

$$\psi(z) = \begin{cases} a\exp(ik_1 z) + b\exp(-ik_1 z), & (z < 0) \\ c\exp(ik_2 z) + d\exp(-ik_2 z), & (0 < z < L), \\ e\exp(ik_1 z), & (z > L) \end{cases} \qquad (5.17)$$

with $E_z = \frac{\hbar^2 k_1^2}{2m_1} = \frac{\hbar^2 k_2^2}{2m_2} + V_0$, where m_1 (m_2) are the electron effective mass outside (in) the barrier and V_0 is the barrier height. The relation between the amplitude coefficients (a, b, c, d, e) are given by the continuity requirement of ψ and $\frac{1}{m}\frac{d\psi}{dz}$ at $z = 0$ and L[100]. The transmission probability is thus given as

$$T(E_z, V_0) = \left[1 + (\frac{v_1^2 - v_2^2}{2v_1v_2})^2 sin^2 k_2 L\right]^{-1} \text{ for } E_z > V_0, \tag{5.18}$$

$$T(E_z, V_0) = \left[1 + (\frac{v_1^2 + u_2^2}{2v_1u_2})^2 sinh^2 \kappa_2 L\right]^{-1} \text{ for } E_z < V_0, \tag{5.19}$$

with $v_1 = k_1/m_1$, $v_2 = k_2/m_2$, $\kappa_2 = \sqrt{2m_2(V_0 - E_z)/\hbar^2}$, and $u_2 = \kappa_2/m_2$.

In Fig. B4.1(b), $T(E_z, V_0)$ with $V_0 = 0.6$ eV (InAs-InP conduction band offset), and $m_1 = 0.026\ m_e$ from InAs, $m_2 = 0.08\ m_e$ from InP[24] is shown.

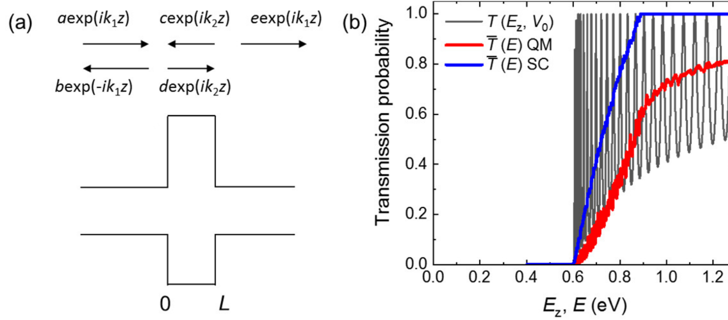

Figure B4.1: (a) Schematic illustration of the incident, reflected, and transmitted electron waves for a time-independent wave function across an energy barrier. (b) The calculated 1D quantum mechanical transmission probability $T(E_z, V_0)$ (gray) and the total quantum mechanical (red) and semiclassical (blue) transmission probability $\overline{T}(E)$ over a rectangular barrier.

In a nanowire, the total kinetic energy of electrons E can be expressed as

$$E = E_z + E_{x,y} = E_z + \frac{\hbar^2 k_{x,y}^2}{2m} = E_z + \epsilon_n, \tag{5.20}$$

where $E_{x,y}$, $k_{x,y}$, and E_n (with n = 1, 2, 3, …) are the energy, wavevector, and quantized energy levels in the cross-section. In a planar heterostructure, the lateral momentum is conserved, thus for electrons with total kinetic energy E, the average transmission probability $\overline{T}$ can be expressed as

$$\overline{T} = \sum_{n=1}^{N} T(E - E_n, V_{0,n})\,/N, \tag{5.21}$$

where E_{N+1} is the lowest state with $E_{N+1} > E$ and

$$V_{0,n} = V_0 + \left(E_{n,InP} - E_{n,InAs}\right) = V_0 + \frac{\hbar^2 k_n^2}{2}\left(\frac{1}{m_2} - \frac{1}{m_1}\right). \tag{5.22}$$

$\overline{T}(E)$ for an InAs nanowire with a square cross-section with 60 nm side lengths and an InP barrier with $L = 60$ nm is shown in Fig. B4.1 (b).

In contrast, the **semiclassical transmission model** assumes that the transmission is equal to 1 if the energy and lateral momentum are conserved at the heterojunction, i.e.[39,99]

$$\frac{\hbar^2 k_1^2 + k_{x,y}^2}{2m_1} = \frac{\hbar^2 k_2^2 + k_{x,y}^2}{2m_2} + V_0. \quad (5.23)$$

$\overline{T}(E)$ calculated based on the semiclassical transmission model is shown in Fig. B4.1 (b) for comparison. Moreover, if the energy quantization in the nanowire cross-sections is neglected, an analytical expression for $\overline{T}(E)$ can be derived from Eq. 5.23 as

$$\overline{T}(E) = 1 - \sqrt{1 - \frac{m_2}{m_1}\frac{E - V_0}{E}}, \quad (5.24)$$

for $V_0 < E < \frac{m_2}{m_2 - m_1} V_0$, $T(E) = 0$ for $E < V_0$, and $T(E) = 1$ for $E > \frac{m_2}{m_2 - m_1} V_0$.

The internal quantum efficiency, defined as the ratio of the number of electrons collected by the contact ($\approx I_p/e$) to the number of absorbed photons[98], is thus determined by hot-electron relaxation in the emitter and the transmission across the barrier. To increase the internal quantum efficiency, hot-electron relaxation in the emitter can be reduced by decreasing the distance between photon absorption and the barrier so that the electron traverse time is short compared to the electron-electron and electron-phonon inelastic scattering time, which can also be increased through material engineering [101,102]. Also, the transmission probability can be optimized by matching the barrier height with hot-electron energy, relaxing the lateral momentum conservation through using nonplanar barriers[103] or, as indicated in Eq. 5.24, through utilizing heterostructures with large effective mass ratio m_2/m_1.

The energy barrier and thus the barrier transmission probability are however modified when a bias V is applied. Thus the total current $I(V)$ can be expressed as

$$I(V) = I_P(V) + I_R(V), \quad (5.25)$$

where $I_R(V)$ is the reverse dark current. For $I_R \ll I_P$, as in Paper V, the open circuit condition simplifies to $I(V) \approx I_P(V) = 0$. Thus, if the energy distribution of the electron flux at the barrier interface $n(E, \hbar\omega)$ is similar to the energy distribution of the photo-excited electrons, the open circuit condition is achieved approximately when

$$V_0 + V = \frac{m_{\mathrm{h,InAs}}}{m_{\mathrm{e,InAs}} + m_{\mathrm{h,InAs}}}(\hbar\omega - E_g), \quad (5.26)$$

as shown in Fig. 5.7 (b)[70,104]. The open circuit voltage V_{OC} is a measure of the average maximum work each electron can perform on the external load[105].

5.4.2 Photo-thermionic emission effect

When the photo-excited electrons and the background electrons are fully thermalized, the energy dependent occupation number is described by the Fermi-Dirac distribution $f(T,\mu)$ with a well-defined temperature T and (quasi-)Fermi level μ. Some thermally excited electrons with $E > V_0$ can be emitted across the barrier through thermionic emission (Fig. 5.8). Thus, a photocurrent can be generated even when the energy of the photo-excited electrons and holes is below the barrier. If the electron transport is ballistic in the barrier, the photo-thermionic emission current can be expressed as

$$I = e\int v_z D(E)\bar{T}(E)(f(T,\mu) - f(T_0,\mu_0))dE, \tag{5.27}$$

If $\bar{T}(E)$ is calculated based on the semiclassical transmission model with a uniform electron effective mass, Eq. 5.27 simplifies to the well-known thermionic current expression in Eq. 3.10[39].

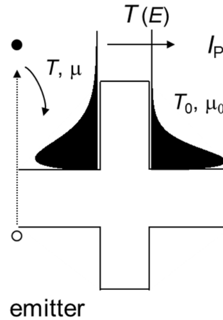

Figure 5.8: Schematic illustration of the photo-thermionic effect. The photocurrent is generated through the thermionic emission of the thermalized hot electrons in the emitter.

Similar to the internal photoemission effect, the internal quantum efficiency of the photo-thermionic emission effect can also be increased through optimizing the barrier transmission probability and reducing hot-electron relaxation through electron-phonon scattering, but the efficiency is not decreased due to electron-electron scattering, which is required to establish thermalized electron distributions.

Chapter 6

Conclusion and outlook

In this thesis, we investigated electron transport in semiconductor nanowires where the electronic properties are modulated through crystal phase engineering, quantum confinement, and band engineering of heterostructures. In particular, we focused on the transport of electrons that are thermally or optically excited. Thermoelectric and photovoltaic effects were studied, where thermally and optically induced nonequilibrium electron distributions lead to the production of electricity.

In semiconductor nanowires, heterostructures with atomically sharp interfaces can be formed through crystal structure engineering[8,14]. Nanowires of InAs are of particular interest for electronic applications due to their favourable bulk properties, such as high mobility, high injection velocities, and low contact resistance [23,106–109]. Electronic properties of InAs ZB/WZ heterostructures, including band offset, polarization charge, and carrier concentrations, were extracted in this thesis. As nanowires often contain a high density of stacking defects and polytypism, this information is important for nanowire transistor research, and for multitude of quantum transport studies [110,111] employing InAs nanowires. In addition, it can be used to interpret and simulate transport effects in crystal phase-defined quantum dots as studied in ref.[8,27] and Paper II. Furthermore, the activation energy barrier formed by including a WZ segment in an InAs ZB nanowire can be tuned between 0 and 300 meV, which is an optimal range for studying energy filtering that can be used to enhance the thermoelectric power factor near room temperature [103,112].

Also in the thesis, the thermoelectric power factor limit for a non-ballistic 1D channel was derived based on the quantum bound of thermoelectric power output[56,57], and tested experimentally in InAs nanowire devices. 1D nanowires

have long been considered as a promising candidates for thermoelectrics[45,113]. The theoretical limit proposed in this thesis provides a clear guideline on the material properties required to achieve high thermoelectric power output density and energy conversion efficiency. Particularly, the theoretical limit shows that state-of-the art semiconductor nanowires with small cross section and high crystal quality as shown in ref.[114] can be expected to have a highly competitive power factor (on the order of mW/m K^2) at low temperatures in comparison to bulk materials. In addition, the thermoelectric study of non-ballistic 1D channels in this thesis can serve as a reference for future experiment that uses the thermoelectric response as a probe of the transport physics of (quasi-) 1D and 0D systems.

Optical hot carrier devices, in which electrons and holes with high kinetic energies are extracted to produce electricity, share much underlying physics with thermoelectric effects. In fact, the power production in hot-carrier solar cells can, in some cases, be considered as a combination of the photovoltaic (quasi-Fermi level splitting) and the thermoelectric effects[65]. The optically excited hot-electrons can however have much higher kinetic energies and highly non-equilibrium distributions. The nanowire- metal plasmonic antenna device demonstrated in this thesis is an ideal platform to study the transport of such hot-electrons as they can be efficiently generated in a localized spot controlled by the position of the nanoantenna and with energies controlled by the wavelengths of the incident light. In addition, the optical hot-carrier devices also provide new photodetection functionalities, for example photo-thermionic emission. Such emission is roughly proportional to $\exp(-V_0/k_B T)$ and is therefore extremely sensitive to the peak temperature of the hot electrons, and can be used to extract the duration of incident laser pulses. Moreover, the nanophotonic effects in both semiconductor nanowires and metal plasmonic structures offer a wealth of opportunities to engineer novel optical responses. Finally, as the number of background mobile electrons and optically excited hot-electrons within a single nanowire can vary from 1000s down to just a few, thus, in contrast to planar devices, single nanowire-based hot-carrier devices illuminated with pulsed laser can be used to study stochastic thermodynamics.

Bibliography

1. D. Cheung, E. Brach, *Conquering the Electron: The Geniuses, Visionaries, Egomaniacs, and Scoundrels Who Built Our Electronic Age* (Littlefield Publishers, 2014).
2. R. T. R., *The Chip: How Two Americans Invented the Microchip and Launched a Revolution* (Paw Prints, 1984).
3. E. Kaxiras, *Atomic and Electronic Structure of Solids* (2003).
4. N. W. Ashcroft, N. D. Mermin, *Solid State Physics* (California, 1976).
5. D. V. Schroeder, *An Introduction to Thermal Physics* (Addison Wesley, 1999).
6. S. Datta, *Electronic Transport in Mesoscopic Systems* (1997).
7. J.-P. Colinge, J. C. Greer, *Nanowire Transistors: Physics of Devices and Materials in One Dimension* (Cambridge University Press, 2016).
8. K. A. Dick, C. Thelander, L. Samuelson, P. Caroff, Crystal phase engineering in single InAs nanowires. *Nano Lett.* **10**, 3494–3499 (2010).
9. K. A. Dick *et al.*, Control of III–V nanowire crystal structure by growth parameter tuning. *Semicond. Sci. Technol.* **25**, 024009 (2010).
10. C. F. Bohren, D. R. Huffman, *Absorption and Scattering of Light by Small Particles* (1998).
11. L. Cao *et al.*, Engineering light absorption in semiconductor nanowire devices. *Nat. Mater.* **8**, 643–647 (2009).
12. K. A. Dick, A review of nanowire growth promoted by alloys and non-alloying elements with emphasis on Au-assisted III–V nanowires. *Prog. Cryst. Growth Charact. Mater.* **54**, 138–173 (2008).
13. D. Ercolani *et al.*, InAs/InSb nanowire heterostructures grown by chemical beam epitaxy. *Nanotechnology*. **20**, 505605 (2009).
14. S. Lehmann, J. Wallentin, D. Jacobsson, K. Deppert, K. A. Dick, A General

Approach for Sharp Crystal Phase Switching in InAs, GaAs, InP, and GaP Nanowires Using Only Group V Flow. *Nano Lett.* **13**, 4099–4105 (2013).

15. H. Kriaa, A. Guitton, N. Maloufi, Fundamental and experimental aspects of diffraction for characterizing dislocations by electron channeling contrast imaging in scanning electron microscope. *Sci. Rep.* **7**, 9742 (2017).
16. S. Fahlvik Svensson *et al.*, Control and understanding of kink formation in InAs–InP heterostructure nanowires. *Nanotechnology*. **24**, 345601 (2013).
17. G. Benenti, G. Casati, K. Saito, R. S. Whitney, Fundamental aspects of steady-state conversion of heat to work at the nanoscale. *Phys. Rep.* **694** (2017), pp. 1–124.
18. F. Menges *et al.*, Temperature mapping of operating nanoscale devices by scanning probe thermometry. *Nat. Commun.* **7**, 10874 (2016).
19. D. G. Cahill *et al.*, Nanoscale thermal transport. *J. Appl. Phys.* **93**, 793–818 (2003).
20. F. Menges, H. Riel, A. Stemmer, B. Gotsmann, Nanoscale thermometry by scanning thermal microscopy. *Rev. Sci. Instrum.* **87**, 074902 (2016).
21. D. Kriegner *et al.*, Unit cell structure of crystal polytypes in InAs and InSb nanowires. *Nano Lett.* **11**, 1483–1489 (2011).
22. P. Caroff, J. Bolinsson, J. Johansson, Crystal Phases in III--V Nanowires: From Random Toward Engineered Polytypism. *IEEE J. Sel. Top. Quantum Electron.* **17**, 829–846 (2011).
23. C. Thelander, P. Caroff, S. Plissard, A. W. Dey, K. A. Dick, Effects of crystal phase mixing on the electrical properties of InAs nanowires. *Nano Lett.* **11**, 2424–2429 (2011).
24. A. Belabbes, C. Panse, J. Furthmüller, F. Bechstedt, Electronic bands of III-V semiconductor polytypes and their alignment. *Phys. Rev. B*. **86**, 1–12 (2012).
25. A. De, C. E. Pryor, Predicted band structures of III-V semiconductors in the wurtzite phase. *Phys. Rev. B*. **81**, 155210 (2010).
26. A. Belabbes, J. Furthmüller, F. Bechstedt, Relation between spontaneous polarization and crystal field from first principles. *Phys. Rev. B*. **87**, 035305 (2013).
27. M. Nilsson *et al.*, Single-electron transport in InAs nanowire quantum dots formed by crystal phase engineering. *Phys. Rev. B*. **93**, 195422 (2016).
28. S. A. Dayeh, D. Susac, K. L. Kavanagh, E. T. Yu, D. Wang, Structural and Room-Temperature Transport Properties of Zinc Blende and Wurtzite InAs Nanowires. *Adv. Funct. Mater.* **19**, 2102–2108 (2009).
29. M. Murayama, T. Nakayama, Chemical trend of band offsets at

wurtzite/zinc-blende heterocrystalline semiconductor interfaces. *Phys. Rev. B*. **49**, 4710–4724 (1994).

30. M. Hjort *et al.*, Electronic and structural differences between wurtzite and zinc blende inas nanowire surfaces: Experiment and theory. *ACS Nano*. **8**, 12346–12355 (2014).

31. R. Timm *et al.*, Interface composition of atomic layer deposited HfO2 and Al2O3 thin films on InAs studied by X-ray photoemission spectroscopy. *Microelectron. Eng.* **88**, 1091–1094 (2011).

32. C. Thelander *et al.*, The electrical and structural properties of n-type InAs nanowires grown from metal-organic precursors. *Nanotechnology*. **21**, 9 (2010).

33. B. Bauer *et al.*, Direct detection of spontaneous polarization in wurtzite GaAs nanowires. *Appl. Phys. Lett.* **104**, 211902 (2014).

34. W. Colin, D. Jena, *Polarization Effects in Semiconductors From Ab Initio Theory to Device Applications* (Springer US, 2008).

35. T. T. Heikkilä, *The Physics of Nanoelectronics* (Oxford University Press, 2013).

36. M. Lundstrom, *Fundamentals of Carrier Transport* (Cambridge University Press, 2002).

37. K. Horio, H. Yanai, Numerical Modeling of Heterojunctions Including the Thermionic Emission Mechanism at the Heterojunction Interface. *IEEE Trans. Electron Devices*. **37**, 1093–1098 (1990).

38. K. Yang, J. R. East, G. I. Haddad, Numerical modeling of abrupt heterojunctions using a thermionic-field emission boundary condition. *Solid State Electron.* **36**, 321–330 (1993).

39. R. Kim, C. Jeong, M. S. Lundstrom, On momentum conservation and thermionic emission cooling. *J. Appl. Phys.* **107**, 054502 (2010).

40. T. Grosges, A. Vial, D. Barchiesi, Models of near-field spectroscopic studies: comparison between Finite-Element and Finite-Difference methods. *Opt. Express*. **13**, 8483 (2005).

41. "The Finite Element Method (FEM)," https://www.comsol.com/multiphysics/finite-element-method.

42. R. Lake, S. Datta, Energy balance and heat exchange in mesoscopic systems. *Phys. Rev. B*. **46**, 4757–4763 (1992).

43. L. P. Kouwenhoven *et al.*, in *Mesoscopic Electron Transport* (Springer Netherlands, Dordrecht, 1997), pp. 105–214.

44. C. W. J. Beenakker, Theory of Coulomb-blockade oscillations in the conductance of a quantum dot. *Phys. Rev. B*. **44**, 1646–1656 (1991).

45. L. D. Hicks, M. S. Dresselhaus, Thermoelectric figure of merit of a one-dimensional conductor. *Phys. Rev. B*. **47**, 16631–16634 (1993).

46. N. T. Hung, E. H. Hasdeo, A. R. T. Nugraha, M. S. Dresselhaus, R. Saito, Quantum Effects in the Thermoelectric Power Factor of Low-Dimensional Semiconductors. *Phys. Rev. Lett.* **117**, 036602 (2016).

47. K. Nishiyama *et al.*, A comparative study of suturing techniques in microlaryngosurgery. *Acta Otolaryngol. Suppl.* **45**, 72–4 (2002).

48. H. J. Goldsmid, *The Physics of Thermoelectric Energy Conversion* (IOP Publishing, 2017).

49. H. van Houten, L. W. Molenkamp, C. W. J. Beenakker, C. T. Foxon, Thermo-electric properties of quantum point contacts. *Semicond. Sci. Technol.* **7**, B215–B221 (1992).

50. J. Davies, The Physics of Low-Dimensional Semiconductors. *Cambridge Univ. Press*. **Cambridge** (1998), p. 4.

51. E. Sugawara, H. Nikaido, Properties of AdeABC and AdeIJK efflux systems of Acinetobacter baumannii compared with those of the AcrAB-TolC system of Escherichia coli. *Antimicrob. Agents Chemother.* **58**, 7250–7 (2014).

52. A. Szafer, A. D. Stone, Theory of Quantum Conduction through a Constriction. *Phys. Rev. Lett.* **62**, 300–303 (1989).

53. C. W. J. Beenakker, H. van Houten, Quantum Transport in Semiconductor Nanostructures. *Solid State Phys.* **44**, 1–228 (2004).

54. W. Magnus, W. Schoenmaker, *Quantum Transport in Submicron Devices* (Springer Berlin Heidelberg, Berlin, Heidelberg, 2002), vol. 137 of *Springer Series in Solid-State Sciences*.

55. I. P. Batra, Origin of conductance quantization. *Surf. Sci.* **395**, 43–45 (1998).

56. R. S. Whitney, Most Efficient Quantum Thermoelectric at Finite Power Output. *Phys. Rev. Lett.* **112**, 130601 (2014).

57. R. S. Whitney, Finding the quantum thermoelectric with maximal efficiency and minimal entropy production at given power output. *Phys. Rev. B*. **91**, 115425 (2015).

58. S. Datta, *Quantum Transport: Atom to Transistor* (Cambridge University Press, Cambridge, 2005).

59. J. Shah, *Hot Carriers in Semiconductor Nanostructures* (Elsevier, 1992).

60. A. J. Nozik, G. Conibeer, M. C. Beard, Eds., *Advanced Concepts in Photovoltaics* (Royal Society of Chemistry, Cambridge, 2014), *Energy and Environment Series*.

61. L. C. Hirst, N. J. Ekins-Daukes, Fundamental losses in solar cells. *Prog.*

Photovoltaics Res. Appl. **19**, 286–293 (2011).

62. W. Shockley, H. J. Queisser, Detailed Balance Limit of Efficiency of p□n Junction Solar Cells. *J. Appl. Phys.* **32**, 510–519 (1961).

63. R. T. Ross, A. J. Nozik, Efficiency of hot-carrier solar energy converters. *J. Appl. Phys.* **53**, 3813–3818 (1982).

64. P. Würfel, Solar energy conversion with hot electrons from impact ionisation. *Sol. Energy Mater. Sol. Cells*. **46**, 43–52 (1997).

65. S. Limpert, S. Bremner, H. Linke, Reversible electron–hole separation in a hot carrier solar cell. *New J. Phys.* **17**, 095004 (2015).

66. M. Massicotte *et al.*, Photo-thermionic effect in vertical graphene heterostructures. *Nat. Commun.* **7**, 12174 (2016).

67. J. W. Schwede *et al.*, Photon-enhanced thermionic emission for solar concentrator systems. *Nat. Mater.* **9**, 762–767 (2010).

68. B. Y. Zheng *et al.*, Distinguishing between plasmon-induced and photoexcited carriers in a device geometry. *Nat. Commun.* **6**, 7797 (2015).

69. S. Limpert *et al.*, Single-nanowire, low-bandgap hot carrier solar cells with tunable open-circuit voltage. *Nanotechnology*. **28**, 434001 (2017).

70. F. Wang, N. A. Melosh, Plasmonic energy collection through hot carrier extraction. *Nano Lett.* **11**, 5426–5430 (2011).

71. B. J. E., W. Y. G., in *Handbook of Optics: Fundamentals, techniques, and design, Volume 1* (McGraw-Hill, 1994).

72. R. B. John P. Dakin, *Handbook of Optoelectronics, Second Edition: Concepts, Devices, and Techniques (Volume One)* (CRC Press, 2017).

73. F. Träger, *Springer Handbook of Lasers and Optics* (Springer Berlin Heidelberg, Berlin, Heidelberg, 2012).

74. M. W. Knight, H. Sobhani, P. Nordlander, N. J. Halas, Photodetection with Active Optical Antennas. *Science (80-.).* **332**, 702–704 (2011).

75. P. Berini, Surface plasmon photodetectors and their applications. *Laser Photon. Rev.* **8**, 197–220 (2014).

76. A. Dorodnyy *et al.*, Plasmonic Photodetectors. *IEEE J. Sel. Top. Quantum Electron.* **24**, 1–13 (2018).

77. A. Arash, K. Mustafa, P. Nezih, in *Photodetectors: Materials, Devices and Applications* (Woodhead Publishing, 2015).

78. A. J. Leenheer, P. Narang, N. S. Lewis, H. A. Atwater, Solar energy conversion via hot electron internal photoemission in metallic nanostructures: Efficiency estimates. *J. Appl. Phys.* **115**, 134301 (2014).

79. E. Cubukcu *et al.*, Plasmonic Laser Antennas and Related Devices. *IEEE J. Sel. Top. Quantum Electron.* **14**, 1448–1461 (2008).

80. P. Biagioni, J.-S. Huang, B. Hecht, Nanoantennas for visible and infrared radiation. *Reports Prog. Phys.* **75**, 024402 (2012).

81. S. A. Maier, *Plasmonics: Fundamentals and Applications* (Springer US, New York, NY, 2007).

82. R. L. Olmon *et al.*, Optical dielectric function of gold. *Phys. Rev. B*. **86**, 235147 (2012).

83. E. David R Lide, CRC Handbook of Chemistry and Physics, Internet Version 2005. *CRC Press. Taylor Fr. Boca Rat. FL* (2005).

84. D. E. Aspnes, A. A. Studna, Dielectric functions and optical parameters of Si, Ge, GaP, GaAs, GaSb, InP, InAs, and InSb from 1.5 to 6.0 eV. *Phys. Rev. B*. **27**, 985–1009 (1983).

85. D. J. Griffiths, *Introduction to Electrodynamics* (Pearson Education Limited, 1962).

86. M. L. Brongersma, Y. Cui, S. Fan, Light management for photovoltaics using high-index nanostructures. *Nat. Mater.* **13**, 451–460 (2014).

87. L. Novotny, N. van Hulst, Antennas for light. *Nat. Photonics*. **5**, 83–90 (2011).

88. J. Schneider, "Understanding the Finite-Difference Time-Domain Method" (2010), www.eecs.wsu.edu/~schneidj/ufdtd.

89. F. Wooten, Optical Properties Of Solids. *Acad. Press* (1972).

90. M. Fox, G. F. Bertsch, Optical Properties of Solids. **70**, 1269–1270 (2002).

91. G. Chen, *Nanoscale Energy Transport and Conversion* (CreateSpace Independent Publishing Platform, 2005).

92. J. Shah, *Ultrafast Spectroscopy of Semiconductors and Semiconductor Nanostructures* (Springer Berlin Heidelberg, Berlin, Heidelberg, 1999), vol. 115 of *Springer Series in Solid-State Sciences*.

93. P. Christopher, M. Moskovits, Hot Charge Carrier Transmission from Plasmonic Nanostructures. *Annu. Rev. Phys. Chem.* **68**, 379–398 (2017).

94. D. E. Fulkerson, M. V. Fischetti, S. E. Laux, Comments on "Monte Carlo simulation of transport in technologically significant semiconductors of the diamond and zinc-blende structures. II. Submicrometer MOSFETs" [with reply]. *IEEE Trans. Electron Devices*. **39**, 749–750 (1992).

95. R. Hathwar, M. Saraniti, S. M. Goodnick, Energy Relaxation and Non-linear Transport in InAs Nanowires. *J. Phys. Conf. Ser.* **647**, 012029 (2015).

96. T. Suzuki, H. Takita, C. T. Nguyen, K. Iiyama, Carrier recombination

lifetime in InAs thin films bonded on low- k flexible substrates. *AIP Adv.* **2**, 042105 (2012).

97. J. W. Schwede *et al.*, Photon-enhanced thermionic emission from heterostructures with low interface recombination. *Nat. Commun.* **4**, 1576 (2013).

98. V. V. Afanas'ev, *Internal Photoemission Spectroscopy Preliminary Remarks and Historical Overview* (Elsevier, 2008).

99. C. M. Wu, E. S. Yang, Carrier transport across heterojunction interfaces. *Solid. State. Electron.* **22**, 241–248 (1979).

100. J.-M. Levy-Leblond, Elementary quantum models with position-dependent mass. *Eur. J. Phys.* **13**, 215–218 (1992).

101. G. J. Conibeer, D. König, M. A. Green, J. F. Guillemoles, Slowing of carrier cooling in hot carrier solar cells. *Thin Solid Films*. **516**, 6948–6953 (2008).

102. H. Sakaki, Scattering Suppression and High-Mobility Effect of Size-Quantized Electrons in Ultrafine Semiconductor Wire Structures. *Jpn. J. Appl. Phys.* **19**, L735–L738 (1980).

103. J.-H. Bahk, Z. Bian, A. Shakouri, Electron energy filtering by a nonplanar potential to enhance the thermoelectric power factor in bulk materials. *Phys. Rev. B*. **87**, 075204 (2013).

104. F. Wang, N. A. Melosh, Power-independent wavelength determination by hot carrier collection in metal-insulator-metal devices. *Nat. Commun.* **4**, 1711 (2013).

105. N. K. Elumalai, A. Uddin, Open circuit voltage of organic solar cells: an in-depth review. *Energy Environ. Sci.* **9**, 391–410 (2016).

106. C. Thelander *et al.*, Electron transport in InAs nanowires and heterostructure nanowire devices. *Solid State Commun.* **131**, 573–579 (2004).

107. J. A. del Alamo, Nanometre-scale electronics with III–V compound semiconductors. *Nature*. **479**, 317–323 (2011).

108. D.-H. Kim, J. A. del Alamo, D. A. Antoniadis, B. Brar, Extraction of Virtual-Source Injection Velocity in sub-100 nm III-V HFETs. *2009 IEEE Int. Electron Devices Meet.*, 1–4 (2009).

109. A. C. Ford *et al.*, Diameter-Dependent Electron Mobility of InAs Nanowires. *Nano Lett.* **9**, 360–365 (2009).

110. S. Nadj-Perge, S. M. Frolov, E. P. A. M. Bakkers, L. P. Kouwenhoven, Spin–orbit qubit in a semiconductor nanowire. *Nature*. **468**, 1084–1087 (2010).

111. T. W. Larsen *et al.*, Semiconductor-Nanowire-Based Superconducting Qubit. *Phys. Rev. Lett.* **115**, 127001 (2015).

112. A. Shakouri, Recent Developments in Semiconductor Thermoelectric Physics and Materials. *Annu. Rev. Mater. Res.* **41**, 399–431 (2011).

113. J. P. Heremans, M. S. Dresselhaus, L. E. Bell, D. T. Morelli, When thermoelectrics reached the nanoscale. *Nat. Nanotechnol.* **8**, 471–473 (2013).

114. J. Gooth *et al.*, Ballistic One-Dimensional InAs Nanowire Cross-Junction Interconnects. *Nano Lett.* **17**, 2596–2602 (2017).

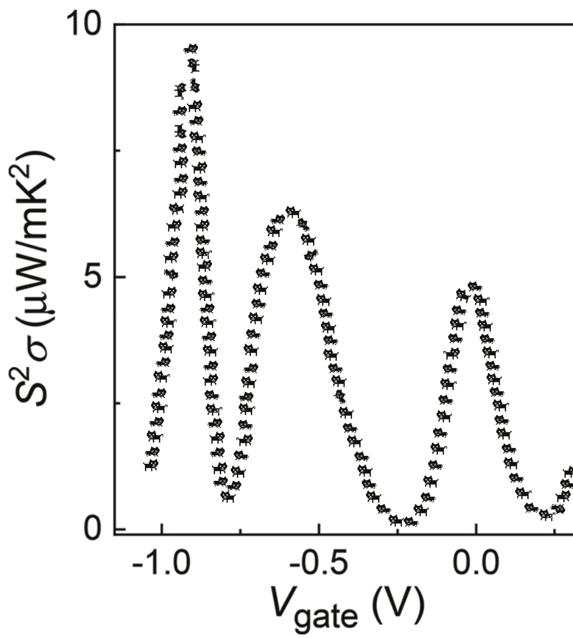

Printed by Media-Tryck, Lund 2018 NORDIC SWAN ECOLABEL 3041 0903

LUND UNIVERSITY

Division of Solid State Physics
Department of Physics
Lund University

ISBN 978-91-7753-794-6